RESEARCH ARTICLE

Key Points:
- The Taan Fiord, Alaska, landslide and deposit volumes are tightly constrained, making this a benchmark subaerial-to-submarine landslide
- We image a blocky landslide deposit on the fjord bottom, which generated a megaturbidite similar to the volume that entered the fjord
- This subaerial-to-submarine landslide deposit has unique characteristics that should allow identification of other such landslides elsewhere

Supporting Information:
- Supporting Information S1
- Data Set S1
- Data Set S2
- Data Set S3
- Data Set S4

Correspondence to:
P. J. Haeussler,
pheuslr@usgs.gov

Submarine Deposition of a Subaerial Landslide in Taan Fiord, Alaska

P. J. Haeussler[1] , S. P. S. Gulick[2] , N. McCall[2] , M. Walton[3] , R. Reece[4] , C. Larsen[5], D. H. Shugar[6] , M. Geertsema[7] , J. G. Venditti[8] , and K. Labay[1]

[1]U.S. Geological Survey, Anchorage, AK, USA, [2]Institute for Geophysics and Department of Geological Sciences, University of Texas at Austin, Austin, TX, USA, [3]U.S. Geological Survey, Santa Cruz, CA, USA, [4]Department of Geology and Geophysics, Texas A&M University, College Station, TX, USA, [5]Geophysical Institute, University of Alaska, Fairbanks, AK, USA, [6]Water, Sediment, Hazards, and Earth-surface Dynamics (waterSHED) Lab, University of Washington, Tacoma, WA, USA, [7]British Columbia Ministry of Forests, Prince George, British Columbia, Canada, [8]Department of Geography, Simon Fraser University, Burnaby, British Columbia, Canada

Abstract A large subaerial landslide entered Taan Fiord, Alaska, on 17 October 2015 producing a tsunami with runup to 193 m. We use LiDAR data to show the slide volume to be 76 + 3/−4 million cubic meters and that 51,000,000 m^3 entered Taan Fiord. In 2016, we mapped the fjord with multibeam bathymetry and high-resolution seismic data. Landslide and postlandslide deposits extend 6 km downfjord, are up to 70 ± 11 m thick, and have a total volume of ~147,000,000 m^3. Seismic data image a blocky landslide unit and two units deposited immediately after the landslide. The blocky landslide unit is ~65,000,000 m^3. We infer it consists dominantly of subaerially derived material and secondarily of fjord floor sediment. The overlying units are likely megaturbidites presumably deposited within minutes to days after the landslide. We infer that these deposits dominantly consist of fjord floor material mobilized and suspended as the slide entered and traveled downfjord. The lower postlandslide unit is up to 35 ± 6 m thick, and the upper unit is up to 12 ± 3 m thick. These deposits are distinctive and will leave a lasting record of the event. This subaerial-to-submarine landslide deposit is distinct from other submarine landslide deposits studied in Alaskan fjords because it has a much greater thickness, larger and more angular blocks, distinctive postlandslide megaturbidites, and a higher-amplitude acoustic signature of the blocky deposit. The tight constraints on the landslide source and deposit volumes, topography, bathymetry, and tsunami runup heights and flow directions should make this a benchmark site for landslide-tsunami models.

Plain Language Summary A giant landslide fell into Taan Fiord, Alaska, on 17 October 2015 and caused a tsunami that ran up 193 m—the fourth highest ever recorded. All 10 of the highest tsunami runups ever recorded were caused by this mechanism of a landslide entering a water body. These events are rare; most occurred more than 60 years ago, and the physical environment before and after the landslide are generally not well documented. In Taan Fiord, Alaska, we collected excellent postlandslide data of the Earth's surface, both above and below sea level. We are able to calculate the volume of the landslide and the volume that entered the fjord. We are able to image the landslide and postlandslide deposits, on and beneath the fjord bottom, up to 6 km away from where it entered the water. These deposits are distinctive in their character, up to 70 m thick, and we anticipate that other such deposits should be recognizable in other fjords. The careful documentation of the physical environment of the fjord before and after the landslide, combined with tsunami runup and flow directions, should make this a place where tsunami modelers can test their models to see if they work correctly.

1. Introduction

Submarine landslides occur on continental margins around the globe, are effective at generating significant tsunamis, and pose considerable risk to some coastal communities (e.g., Bardet et al., 2003; Harbitz et al., 2006; Locat & Lee, 2002; Ward, 2001; Wood & Peters, 2015). Although such landslides occur infrequently, their characteristics are relatively well known (e.g., Hampton et al., 1996; Harbitz et al., 2006; Locat & Lee, 2002; Masson et al., 2006; McAdoo et al., 2000; Nardin et al., 1979). At high-latitude margins, submarine failures often occur in fjords and are commonly sourced from fjord head deltas, which then flow into the deeper parts of fjords, where the sediment is trapped and deposited (Aarseth et al., 1989; Bøe et al., 2003; Lee et al., 2006; L'Heureux et al., 2010; Locat & Lee, 2002). These deposits on fjord bottoms tend to be of relatively uniform
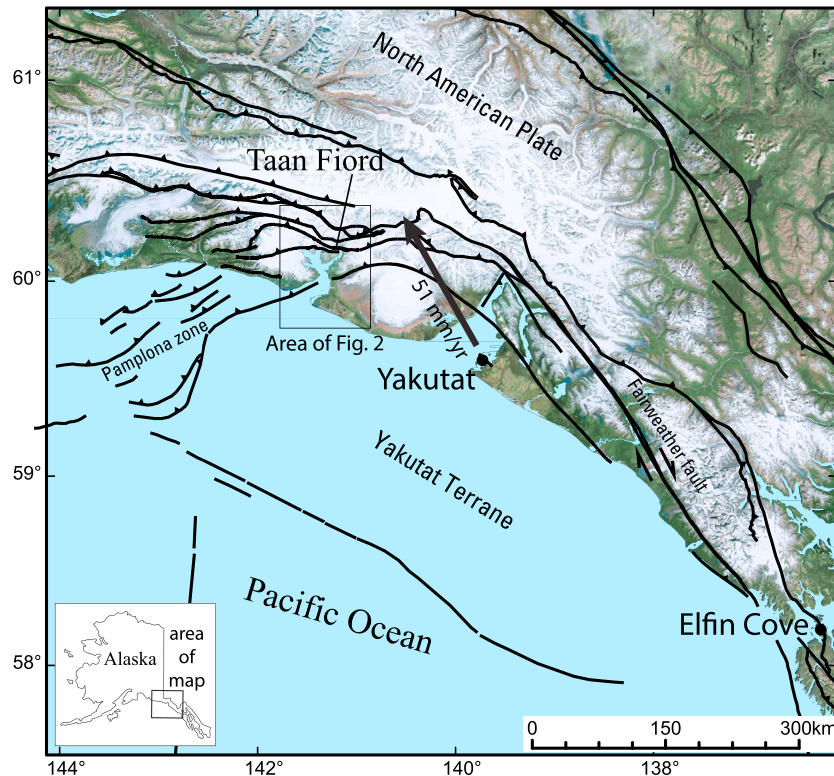
Figure 1. Regional physiographic and tectonic setting of Icy Bay and Taan Fiord. The GPS velocity vector of the Yakutat terrane is shown from Elliott et al. (2013). Active faults, or inferred active faults, are shown, with thrust faults having teeth, and are simplified from Koehler (2013).

thickness and lobate (Aarseth et al., 1989; Haeussler et al., 2007, 2013; Lee et al., 2006; Locat & Lee, 2002; Ryan et al., 2010), as they have a viscous rheology (Jiang & LeBlond, 1992). The acoustic signature of the deposits is commonly transparent or chaotic with low amplitudes. Based on seismic images of submarine landslide deposits, previous studies have imaged erosion at the flow base and evidence that the slide volume grows through inclusion of sediment along the transport path (Aarseth et al., 1989; Brothers et al., 2016; Haeussler et al., 2007, 2013; Hampton et al., 1996; Locat & Lee, 2002; Ryan et al., 2010).

Subaerial landslides that enter bodies of water are particularly effective at generating very large local tsunami. Here we use the shorthand *STS landslide* for a subaerial-to-subaqueous landslide. Tsunami modelers sometimes use the term *landslide tsunami*, *landslide-generated wave*, or the abbreviation *LGW*, for the wave generated by an STS landslide, but that term refers to the wave, not the landslide. The 10 highest tsunami runups documented on Earth were caused by subaerial landslides entering water bodies (Global Historical Tsunami Database, National Geophysical Data Center, NOAA [doi:10.7289/V5PN93H7] last accessed 10 August 2018). Tsunami runup is the height above sea level that water reached. Perhaps the best known of these occurred in 1958 in Lituya Bay, Alaska, in which an M7.8 earthquake triggered a rockfall that slid into a fjord, which caused a world-record tsunami runup of 524 m (Miller, 1960). Despite the dramatic effects of this, and other, STS landslides, there is little known about the geologic record of these landslide deposits that could be used to identify them and aid in assessing this hazard.

We had the rare opportunity to document the mass transfer of a large subaerial-to-submarine landslide, which occurred in Taan Fiord, Alaska, on 17 October 2015. This remarkable landslide produced the fourth-highest tsunami runup ever recorded (Higman et al., 2018). We are unaware of any previous studies that geophysically image a large subaerial-to-submarine landslide deposit. Thus, the signature of such a deposit is heretofore unknown, as are the effects of the landslide on fjord sedimentation. (Note: The U.S. Board of Geographic Names uses the spelling *Fiord* in proper names. We use the more common spelling of *fjord* in this paper, except when using a formal geographic name, such as *Taan Fiord*.) In this paper, we focus on the bathymetric and seismic character of the submarine deposit, and we infer depositional processes based on
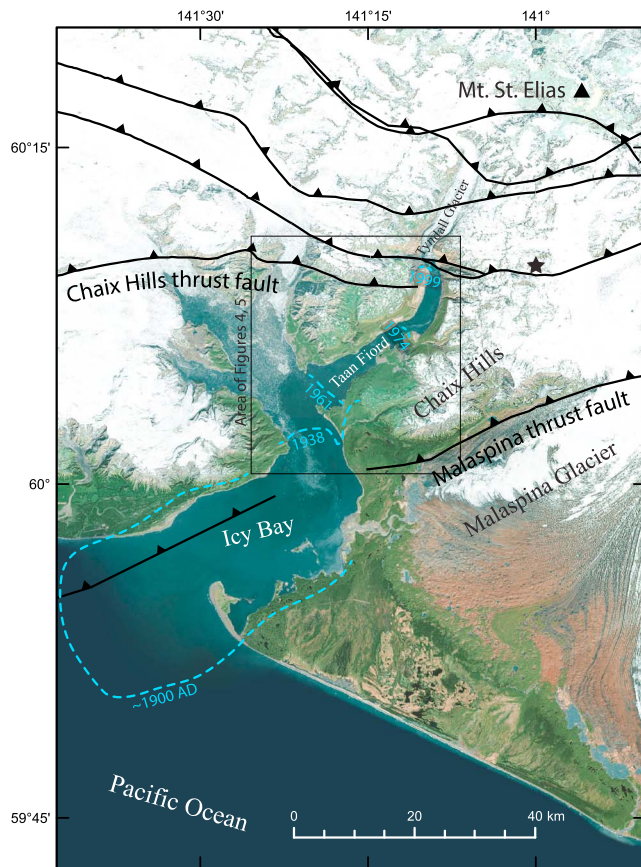
Figure 2. Map showing deglaciation of Icy Bay and Taan Fiord. Known ice positions are shown with dashed white lines from Porter (1989) and Barclay et al. (2006). Star shows inferred location of photographs shown in Figure 3. Active, or inferred active, faults are shown as black lines with teeth from compilation of Koehler (2013).

seismic stratigraphy. We also compare this deposit with purely submarine landslide deposits and show there is a distinct signature of an STS landslide in submarine sediments that may allow their identification elsewhere.

The Taan Fiord STS landslide was first identified from the Global Seismic Network using a long-period seismic detection algorithm (Ekström & Stark, 2013). Subsequently, a tsunami was identified on the tide gauges at the nearest community of Yakutat, about 140-km distance by sea, as well as at Elfin Cove, about 395-km distance by sea (Figures 1 and 2). Satellite images soon after the event also identified the slide, direction of travel, deposition in the fjord, and significant tsunami runup in Taan Fiord. An overview of the Taan Fiord landslide and tsunami is given by Higman et al. (2018) and documents tsunami runup to 193 m. Dufresne et al. (2017) described the subaerial landslide deposits. A model of the subaerial-induced tsunami generation was given by George et al. (2017) with no input from ground-based observations.

Recent retreat of the Tyndall Glacier combined with relatively weak sedimentary rock outcrops, high relief, and rapid tectonic deformation all contributed to preconditioning the slope to failure in Taan Fiord (Higman et al., 2018). Taan Fiord is an arm of Icy Bay, which deglaciated since ~1900 CE (Barclay et al., 2006; Porter, 1989). Photographs of what-is-now Taan Fiord in 1897 shows ice at an altitude of about 350–400 m above today's sea level (Figure 3). The Tyndall Glacier extended to the mouth of what-is-now Taan Fiord around 1961 (Porter, 1989; Figure 2). A 1983 U.S. Geological Survey (USGS) topographic map of this region utilized aerial photographs from 1972 and 1973 and showed ice at an altitude of 250 m above the base of the future landslide. The glacier retreated to a position about half way up the fjord by 1969 (Porter, 1989) and stalled there until about 1983. After subsequent retreat, the glacial terminus reached its current grounded position at sea level around 1999 (Figure 2).

The Icy Bay region includes high relief with the highest coastal mountain in the world, Mount St. Elias (elevation 5,488 m), lying less than 14 km from the shore of Taan Fiord (e.g., Enkelmann et al., 2015). The surface geology in this region consists of weakly lithified sedimentary rock derived from the ongoing collision of the Yakutat microplate with North America (Pavlis et al., 2012). Taan Fiord is in the hanging wall of the Malaspina thrust fault (Pavlis et al., 2012), which essentially connects the Alaska-Aleutian megathrust to the Fairweather fault system via the offshore Pamplona Zone (Gulick et al., 2013; Worthington et al., 2010). Shortening across the Malaspina thrust fault has a GPS-determined shortening rate of about 10 mm/year (Elliott et al., 2013). At the head of Taan Fiord lies the Chaix Hills thrust fault, which has a GPS-determined slip rate of approximately 17 mm/year (Elliott et al., 2013). Thermochronology studies show that rocks in Taan Fiord have been uplifting rapidly at a rate of 2–5 mm/year for >1 Myr (Enkelmann et al., 2015). All these factors contribute to steep and high topography that is prone to landslides. However, the recent glacial retreat, or fluctuations in ice volume, which debuttresses the fjord walls, is perhaps the most significant factor (Grämiger et al., 2017). Lastly, we note that Meigs et al. (2006) mapped an earlier rotational slide at the location of the 2015 landslide and anticipated its future failure.

2. Methods and Data

The 2015 landslide and tsunami provided a unique opportunity to document and study the effect of an STS landslide. A large group of researchers coalesced with the goal to document the event and collect ephemeral and time-sensitive observations (e.g., Dufresne et al., 2017; Higman et al., 2018). This paper focuses on the submarine observations of bathymetry, high-resolution submarine seismic profiling, and surface change. No submarine cores were collected during this study, so all inferences of sedimentary processes are derived from geophysical imaging.
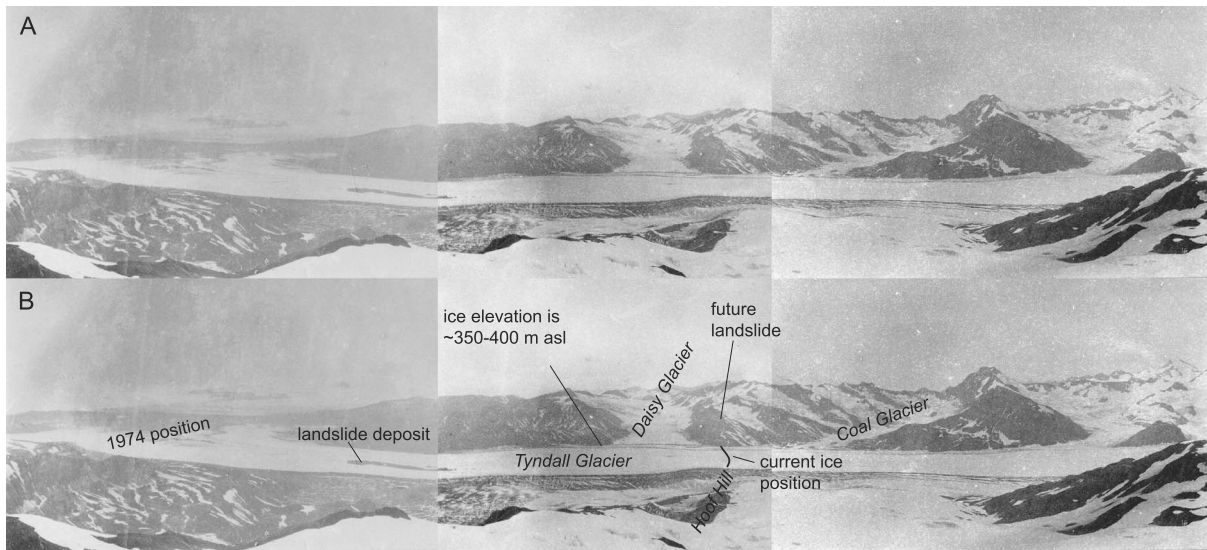
Figure 3. Panorama of Tyndall Glacier in 1897 described as taken from the "top of the Chaix Hills," which we infer to be at the location of the star on Figure 2, or approximately 60.1711°N, 141.0476°W. (a) Uninterpreted and (b) interpreted. Note the landslide debris on the medial moraine. Photographs were taken during the H. G. Bryant expedition to climb Mount St. Elias, and original photographs are in the American Alpine Club library in Golden, Colorado. Comparison of these photographs to present topography indicates ice was roughly 350–400 m above sea level in the area where the slide occurred.

We collected a comprehensive topography and bathymetry data set from Taan Fiord in the summer of 2016, 7 to 10 months after the landslide, with the goal of understanding the mass movement and processes (Figures 4a and 5; supporting information S1). An overview of these data sets and methodology is provided here, but details about each survey are given in the supporting information. A comprehensive multibeam data set was collected onboard the USGS R/V *Alaskan Gyre* using a Reson SeaBat T50-P multibeam echo sounder, which covered the entire area of Taan Fiord, excepting most areas shallower than ~10 m. This data set covers about 99% of the fjord area and was cleaned and gridded to 1-m resolution. Bathymetry in the northern part of the fjord closest to the landslide was also surveyed by an unmanned surface vehicle (USV *Jökull*) using a Teledyne Odom MB2 multibeam echo sounder, which was able to work closer to the shore, and these data were also cleaned and gridded at 1-m resolution. For both surveys, sound velocity profiles were collected to correct the data for water density effects, and tidal corrections were applied utilizing a locally deployed tide gauge.

For topography, we collected a comprehensive LiDAR data set in May of 2016 for the region surrounding Taan Fiord (Figure 4a). These data were collected using a system based on a Riegl LMS-Q240i Pulsed Scanning Altimeter in a swath that was generally 550 m wide at 500 m above ground level, with a density of one point per square meter and a vertical accuracy of about 8 cm. The data were gridded at 1-m resolution. The shoreline of Taan Fiord was digitized from aerial photographs that were collected as the LiDAR was flown. As there were no ground control points, an ellipsoid correction was made from a survey of the tide gauge in Yakutat (see supporting information S1).

We produced a combined bathymetry and topography data set of Taan Fiord (Figure 5; supporting information S1). The LiDAR data extend to the digitized shoreline, and we clipped the topography data at the shoreline. Given the larger area of coverage of the Alaskan Gyre bathymetry data set and cleaner data quality, we utilize the Jökull data between the shallowest extent of the Alaskan Gyre data and the shoreline in the northern part of the fjord (Figure 4a). Gaps remained between the shoreline and the shallowest bathymetry data, which were filled using a natural neighbor interpolation. The final combined topography and bathymetry digital elevation model (DEM) is gridded at 1-m resolution (Figure 5).

Prelandslide topography and bathymetry data sets are of sufficient quality to compare the postlandslide data. For topography, we use a 5-m DEM available from the USGS National Map (https://nationalmap.gov/elevation.html). This DEM was produced from IfSAR data collected between 14 August and 8 September 2012. The elevations were initially relative to ellipsoid Geoid09, and we converted them to Geoid12B to compare to
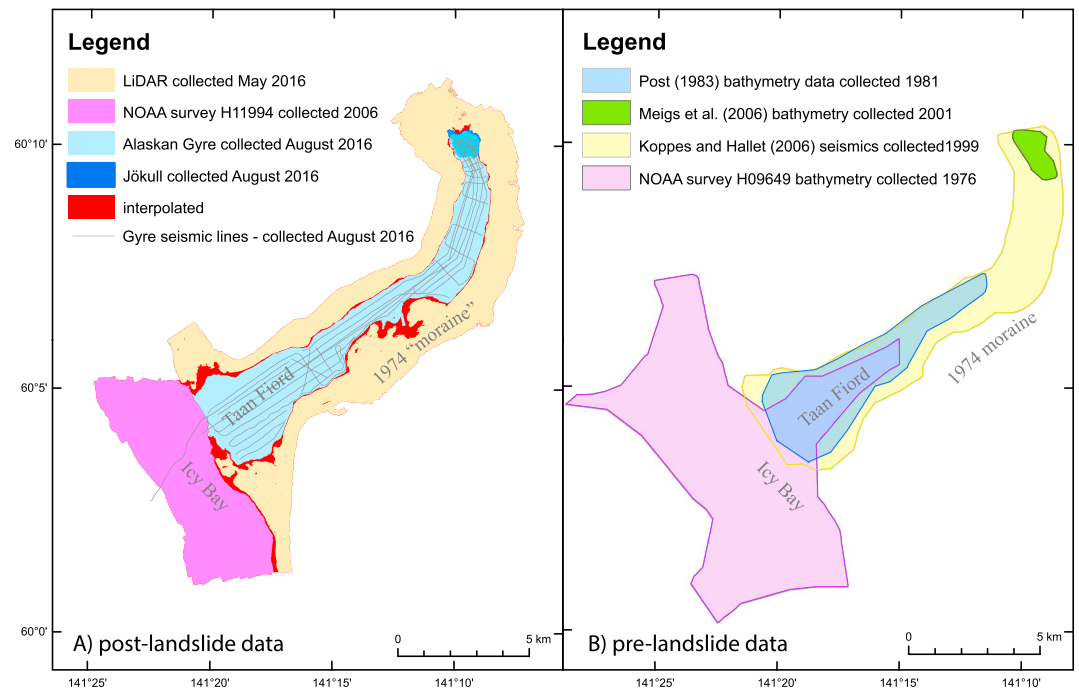
Figure 4. Prelandslide and postlandslide data sets and spatial coverage. (a) Postlandslide elevation and seismic data coverage showing sources discussed in the text and the supporting information as well as areas where depth was extrapolated between the shoreline and the shallowest multibeam data. Both the *Alaskan Gyre* and the *Jökull* surveyed the north end of the fjord, with the light blue color showing the overlap. Also shown are the seismic lines collected on the R/V Alaskan Gyre. Note the NOAA 2006 multibeam survey is prelandslide, but it does not extend into Taan Fiord. As we saw no evidence for bathymetric changes in this area related to the 2015 landslide and tsunami, we combined this data set with our postlandslide bathymetry data sets. (b) Prelandslide bathymetry data coverage—showing areas surveyed by NOAA in 1976 in survey H09649, surveyed by Post (1983) in 1981, surveyed by Koppes and Hallet (2006) in 1999, and surveyed by Meigs et al. (2006) in 2001.

the LiDAR data. The prelandslide shoreline and land cover were also well imaged on a WorldView2 image from 1 March 2014 (image: WV02_20140301_103001002D519500_103001002E3B9600_seg1). The first postlandslide image was a GeoEye image from 25 October 2015 (image: GE01_20151025204441_1050010001C98F00_15OCT25204441_P002).

Earlier bathymetry data sets were collected in parts of Taan Fiord before the landslide in 1976, 1981, 1999, and 2001 (Figure 4b). In 1976 NOAA collected single-beam bathymetry (as part of survey H09649) only in the southwestern basin, as the ice front was still about halfway down the fjord (Figure 2). Post (1983) also collected single-beam soundings in this region in 1981. After retreat of the glacier to its present position, Koppes and Hallet (2006) collected boomer-source high-resolution seismic reflection data throughout the fjord in 1999, which had good penetration, and they used it to produce a bathymetry map, which shows the fjord has a northern and southwestern basin (see Figures 2 and 4 in Koppes & Hallet, 2006). We attempted to manually georegister a grid of their coastline with the modern coastline, but it did not fit well. We also had difficulty forcing the location of the gridded data to lie between the coastlines. Despite considerable effort, we could not resolve the projection issues of the derivative grid with the coastline of the fjord. We also compared these depth data with the Alaskan Gyre multibeam bathymetry data in the southwestern basin, where we presumed little postlandslide change. There was a poor agreement of the depths, which resulted in concerns as to the utility of the 2006 data set because of horizontal resolution (2-D profiles projected to 3-D) and lack of water velocity measurements. Thus, we did not use these data for comparison with our data in the north basin. In 2001, Meigs et al. (2006) utilized a Garmin-brand depth sounder to survey the northern 2 km of the fjord (see Figure 8 in Meigs et al., 2006). We found this to be a useful data set for comparison after a few incongruous data points were deleted, which had values several tens of meters shallower than adjacent soundings. They did not apply any corrections to the data for tides or variations in water velocity.
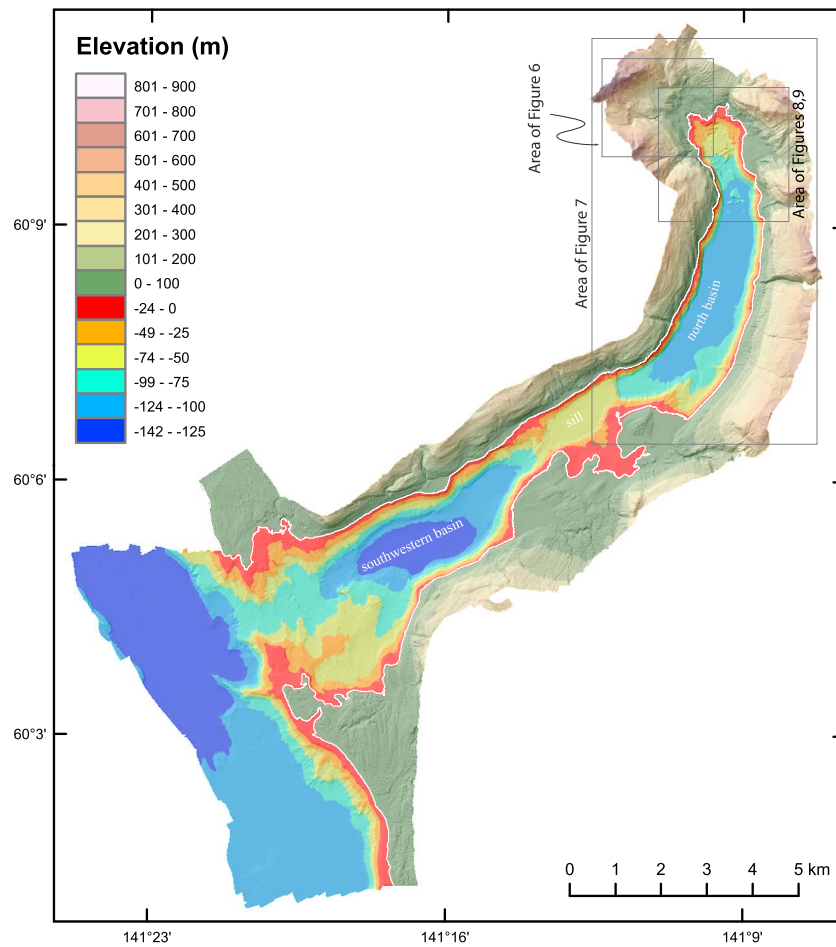
Figure 5. Shaded relief combined postlandslide bathymetry and topography of the 1-m digital elevation model of Taan Fiord. Shoreline or sea level is white line. The methods used to produce the digital elevation model are given in the supporting information S1.

In August 2016, we also collected a suite of high-resolution multichannel seismic data in Taan Fiord (see map in Figure 4a; supporting information S2; doi:10.1594/IEDA/500191 and doi:10.1594/IEDA/500192). The seismic system utilized a 500-J DuraSpark sparker source with a 600-Hz dominant frequency. We used a dual-streamer system including a 24-channel, 72-m active length streamer and an additional 24-channel, 150-m active length streamer. We collected over 450 line kilometers of multichannel seismic data in Taan Fiord and Icy Bay. Additional information on the seismic data acquisition and processing is in the supporting information S2. The theoretical vertical resolution of the data is 1–3 m. We use the velocity of sound in seawater (1,500 m/s) to calculate sediment thickness from the seismic profiles. This velocity approximates fine-grained water saturated sediments and is a value commonly used in seismic reflection studies of fjords (e.g., Cai et al., 1997; Cowan et al., 2010; Hamilton, 1969). Thickness values will be most accurate at shallow depths below the seafloor and will be overestimated when profiles cross bedrock blocks. However, without a straightforward means to correct for this issue, we use the standard 1,500-m/s value. If the true velocity is higher, then all thickness and volume estimates will be higher.

We picked horizons on the seismic reflection data using IHS Kingdom Suite software. We correlated these horizons around the grid of seismic reflection data until we obtained an interpretation that was internally self-consistent for all horizons within the data volume. It is possible that some horizons were picked a half or full cycle off, and we quantify uncertainties in our resultant thickness and volume measurements. Most horizon picks were straightforward, and we were highly confident in their interpreted position. We discuss particular instances where our interpretation was less confident in a following section.

3. Results

3.1. Landslide Source

The minimum volume of the landslide can be estimated by examining the volume difference between the source area before and after the landslide (Table 1; Figure 6a). We find a volume of about 57.7 ± 0.7 million cubic meters for this region by using the CutFill tool in ArcGIS 10.4.1 software to compare the prelandslide and postlandslide surfaces (purple region on left side of Figure 6a). The error in this estimate is from the square root of the sum-of-the-squares (RMS) error (0.75 m) related to vertical accuracy of prelandslide and postlandslide DEMs and their errors (0.74 and 0.08 m, respectively) times the area of the slide. Given that the shoreline did not change significantly below the slide, and that the glacier margin was not deformed below the slide, it appears the toe of the rotational slide did not extend beneath the glacier (see eastern dashed black line on Figure 6a). However, as the slide scar was not completely evacuated of sediment, our computed volume of material that moved during the slide is a minimum. To estimate the volume of material remaining in the slide scar, we inferred an approximate geometry for the base of the landslide from drawing nine cross sections across the slide spaced 100 m apart (like the one shown in Figure 6b; see supporting information S3). This method provides an additional volume of 18.0 + 2.4/−3.6 million cubic meters. To estimate the error in this number we also drew reasonable cross-sectional profiles with the base of the landslide as shallow and deep as plausible and then calculated the volumes. We thus infer the total volume of the material that moved in the source area of the landslide as 75.7 + 3.1/−3.5 million cubic meters (see Table 1).

3.2. Landslide Deposit

The landslide deposit lies above and below sea level (Dufresne et al., 2017; Higman et al., 2018). The subaerial part of the deposit includes the volume within the landslide scar, discussed above, as well as material on the toe of the Tyndall Glacier and the hummocks on the east side of the fjord and on the Hoof Hill fan (Table 1; Figure 7). The area of sediment on the glacier is easily measured from imagery, but the thickness of this sediment was not measured due to the hazard of traveling on the heavily seraced and crevassed glacier. An average sediment thickness of 5 ± 1 m was estimated from observations at the margins of the glacier. The block on the Hoof Hill fan on the east side of the fjord is remarkable in that it demonstrates that sediment transited the entire 1.5-km width of the fjord during the landslide (Dufresne et al., 2017; Higman et al., 2018). This block became known as *Edgar* and is a notable postlandslide landmark visible from around the northern end of the fjord. For further discussion of the hummocks on the east side of the fjord; see Dufresne et al. (2017). The volume of all the subaerially deposited material is calculated from the difference between prelandslide and postlandslide DEMs. These volumes indicate that 33% of the landslide deposit remains on land, including that which initially entered the fjord water and reemerged onland in the area of Hoof Hill, and that 67% of the landslide material entered and remained within the fjord (Table 1).

Much of the submarine landslide deposit is clearly imaged in the bathymetry data (Figures 7 and 8). A block field completely covers the northern 2.5 km of the fjord bottom, and blocks rise above the sea bottom up to 3 km from the shoreline where the landslide entered the water. Note that we use the term *hummocks* for subaerial *blocks* (Paguican et al., 2014) and blocks for their submarine expression to be consistent with the submarine landslide literature. Blocks are up to 300 m across and 35 m above the postlandslide sea bottom. Several 20- to 30-m-tall blocks lie due west of Edgar at the base of the slope, suggesting they were transported together. A group of 20- to 35-m-tall blocks lie in the middle to east side of the fjord, which suggests they were deposited as a group. There is another group of somewhat smaller blocks along the west edge of the fjord. These blocks are 10 to 20 m; they are aligned as a train in the downslope direction and perhaps were deposited as a group. In general, the long axes of blocks approach orientations either perpendicular or parallel to movement, with the highest concentration of parallel blocks along the slide margins (see Figure 6 in Dufresne et al., 2017). The main suite of parallel-to-movement-oriented blocks is on the fjord edge where the least amount of shortening would be expected. The largest block is about 300 m across and 5.7 ha in area (labeled "L" on Figures 8 and 9) and has a more rounded morphology than other blocks, suggesting it consists not of former sedimentary rock outcrop but of sediment. It may be a piece of fjord-bottom sediments that was displaced southward.

A plot of the difference in bathymetry from before and after the landslide reveals additional details about the submarine deposit and processes that occurred during and after the landslide (Figure 9). The 2001 data from Meigs et al. (2006) are detailed and consistent and provide a baseline data set for comparison. The center of

Table 1
Volumes and Areas of Taan Fiord Landslide Deposits

Region	Map area (m^2)	Volume (m^3)	Error (m^3)	Proportion (%)	
Subaerial source					
From difference maps	954,000	57,700,000	±700,000[e]	76	Percent of subaerial slide
Material remaining in slide scar[a,b]	559,000	21,900,000	+2,400,000/ −3,500,000[f]	24	Percent of subaerial slide
Total	1,234,000	75,700,000	+2,500,000/ −3,600,000[g]	100	Percent of subaerial slide
Subaerial deposit					
Material in slide scar and base of slope[b]	559,000	21,900,000	+2,400,000/ −3,500,000[f]		
On glacier[c]	304,000	1,500,000	±300,000[c]		
Blocks on east side of fjord	32,000	1,300,000	±20,000[e]		
Total onland	895,000	24,800,000	+2,500,000/ −3,600,000[g]	33	Percent of subaerial slide
Submarine deposit					
Expected submarine volume[d]	—	50,900,000	—	67	Percent of subaerial slide
Deposits picked from seismics				Percentage relative to subaerial landslide debris that entered the water[e] (%)	Relative to total submarine slide and postslide material (%)
All slide and post-slide material (units BL, PL1, and PL2)	4,547,000	147,500,000	3,900,000[h]	290	100
All blocky material (unit BL)	2,590,000	65,300,000	3,900,000[h]	128	44
Lower postlandslide unit (unit PL1)—megaturbidite	3,639,000	46,400,000	1,800,000[h]	91	31
Upper postlandslide unit (unit PL2)—megaturbidite	3,978,000	29,800,000	1,000,000[h]	58	20
All post-blocky landslide material (sum of units PL1 + PL2)	3,978,000	76,200,000	1,800,000[h]	150	52

[a]Estimate made from nine cross sections through slide. See text for details. [b]Includes material remaining in slide scar (18,000,000 m^3) and volume from topography difference map (3,900,000 m^3). [c]Assumes uniform 5 ± 1-m thickness for entire deposit, area from satellite image of 304,000 m^2. [d]From total volume displaced (75,700,000 m^3) minus total volume onland (24,800,000 m^3), thus 50,900,000 m^3. [e]Square root of the sum of the squares of source digital elevation model errors. [f]Error from picking shallower and deeper *reasonable* slide surfaces. [g]Square root of the sum of the squares of above errors. [h]Square root of the sum of the squares of picking and resolution errors multiplied by area error as described in text.

the fjord between the Hoof Hill fan and the landslide was typically 35 m shallower in 2016 than 2001. The largest shallowing of depth occurred where the large blocks lie. The region just offshore of the toe of the landslide is more than 50 m shallower (Figure 9). However, there are areas with remarkably little change in depth, such as the area on the west side of the fjord about 0.5 km south of the toe of the landslide.

The submerged apron of the Hoof Hill fan has three segments, which show from north to south (a) erosion, (b) dispersed deposition, and (c) focused deposition (Figure 9). The northern 0.5 km of the fan became deeper by up to 15–20 m. We infer that this depth change resulted from the landslide and tsunami, because both the 2001 shoreline mapped by Meigs et al. (2006) and a 2014 satellite image show the shoreline extending up to 73 m farther offshore prior to the landslide (Figure 9).

We interpret the three segments of the Hoof Hill fan as having three different mechanisms for its bathymetry. For the northern part where there was removal of sediment, we speculate this may be from currents related to the landslide causing upward directed water flow or alternatively backflow from sediment draining off the subaerial fan after the tsunami. As the highest tsunami runup (193 m; Higman et al., 2018) is located east of this shoreline, there must have been significant backflow. The present location of the evacuated sediment is not known, as there is no distinctive deposit at the toe of the slope that appears derived from the shallower part of the fan. However, these materials may make up parts of the postlandslide deposits mapped in seismic data downfjord (see following section). A lack of gullies on the submerged fan related to downslope currents suggests to us that the failure of the northern fan front may be related to upward-directed currents, not from backflow. Moreover, the presence of the block Edgar along this part of the fan is strong evidence for upward flow. The middle ~300 m of the Hoof Hill fan shoaled by 10–20 m during the interval between 2001 and 2016. The shoreline prograded 30–45 m westward in this time period. We infer this progradation was caused by dispersed sedimentation across the fan front, because of the relative uniformity of depth changes. Satellite
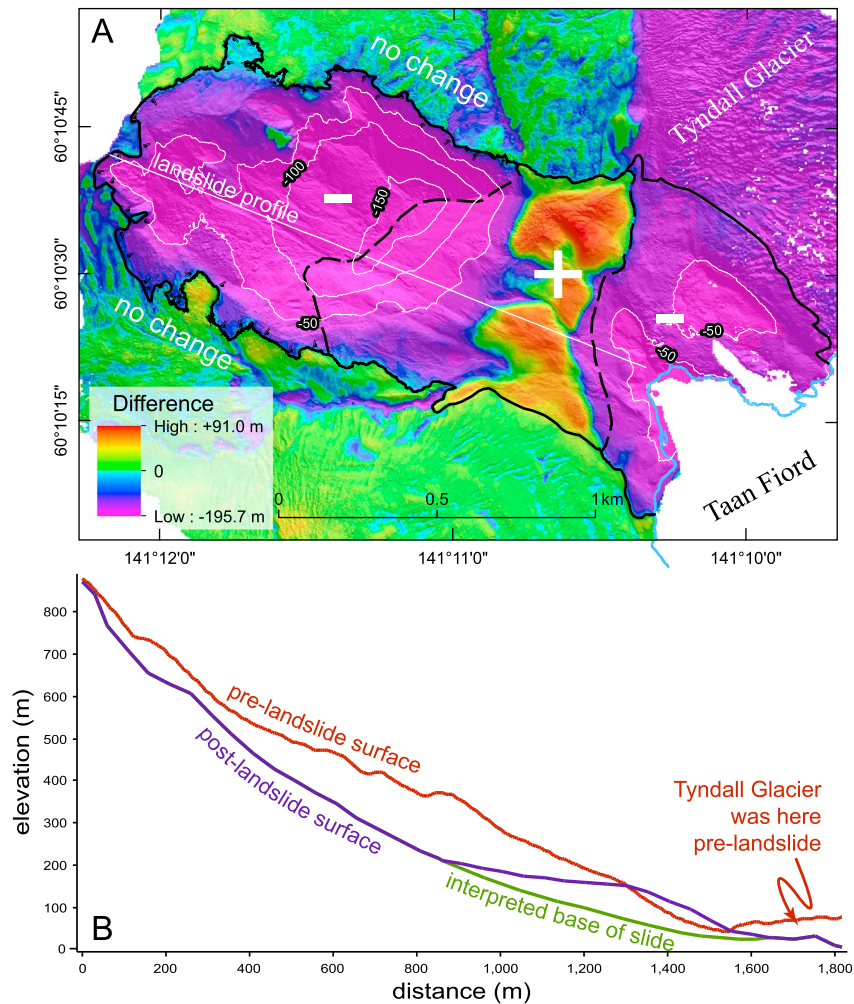
Figure 6. (a) Difference in topography before and after landslide. Purple colors are where topography is lower after the landslide, warm colors are where the topography is higher, and green color is no elevation change. Elevation change is contoured in 50-m intervals. The margin of the landslide, solid black line, is delineated by the zero change-in-elevation contour. The upper and lower limits of slide debris remaining in the slide scar are mapped with dashed black line. Note the Tyndall Glacier has retreated and thinned in the time interval between September 2012 and May 2016, and thus, it is also purple. (b) A profile along the landslide, showing prelandslide and postlandslide surfaces and the interpreted base of landslide. We constructed similar profiles at 100-m intervals across the landslide to reconstruct the volume of material remaining in the slide scar. For clarity, we do not show those profile locations on this figure; however, they are all shown in supporting information S3.

images support this interpretation. Examination of historical imagery using Google Earth shows variability in the amount of vegetation along the fan front, particularly for the middle and southern parts of the fan. The southern 250-m length of the Hoof Hill fan has a shoreline that prograded 70–90 m to the southwest between 2001 and 2016. However, there was no change in the position of the coastline due to the landslide. Moreover, the bathymetry change map shows shoaling in a broad mound-shaped region of up to 65 m (Figure 9). There are no failure scarps, rills, or other evidence of high-velocity currents along this part of the fan, which indicates it escaped the effects of the landslide and tsunami. The 2014 satellite image, as well as a review of Google Earth historical imagery, shows the primary drainage of the Hoof Hill fan is in approximately this southern position, which leads us to consider this region as the locus of deposition for at least the last 20 years. The bathymetry difference map yields an average sedimentation rate of up to 4.3 m/year. Meigs et al. (2006) anticipated continued rapid erosion of the tributary valleys after glacial recession with deposition of sediments on alluvial fans at the fjord margins. These data demonstrate this process but also show that sedimentation is not uniform across the fan face.
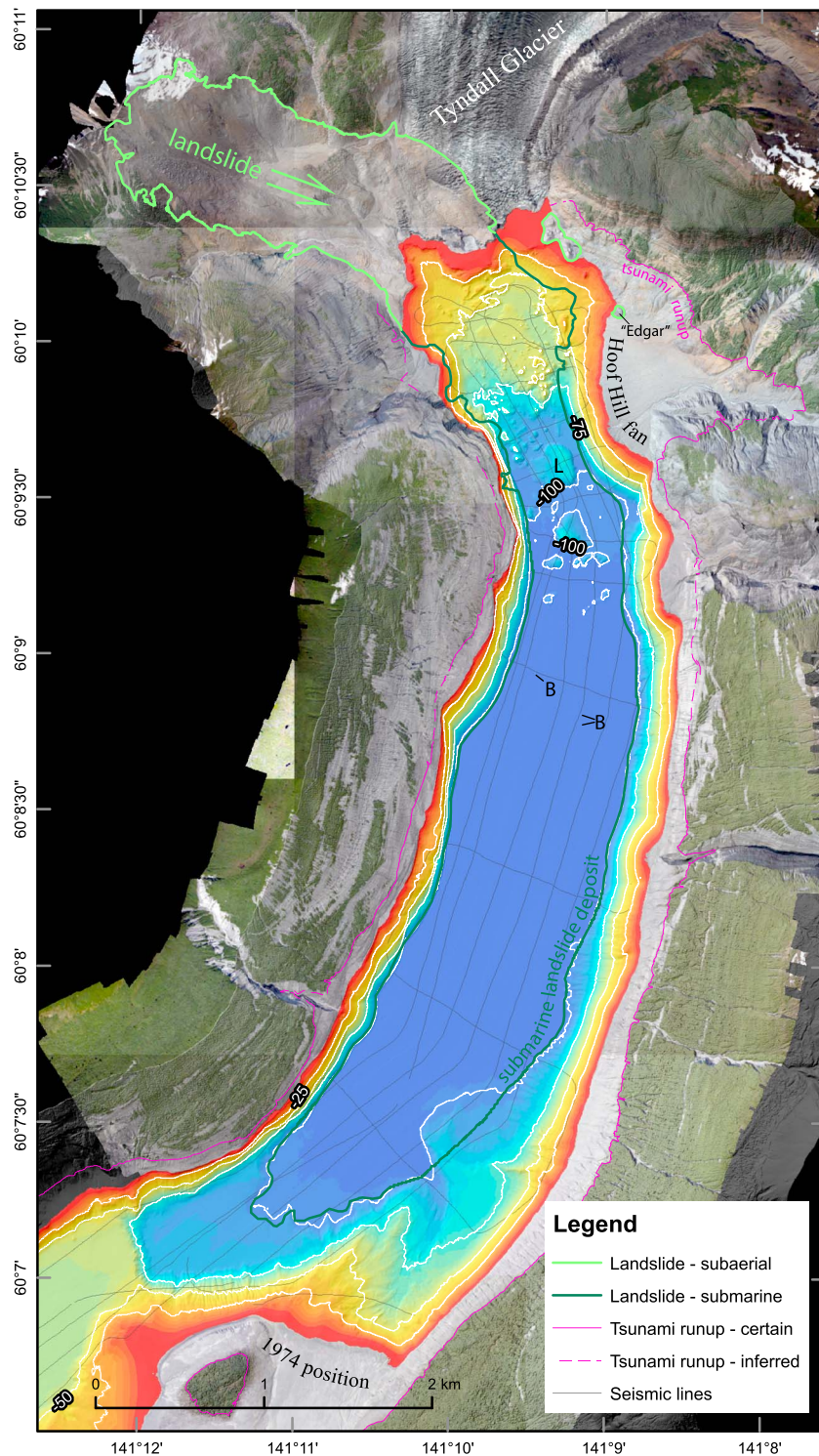
Figure 7. Bathymetry and topography of the north basin of Taan Fiord. A shaded relief digital elevation model of the bathymetry is shown surrounded with color orthophotos taken during acquisition of LiDAR data on 29 May 2016. Small blocks labeled "B" are the furthest from the landslide that barely protrude above the fjord bottom. Largest block labeled "L" is discussed in text.

Since the landslide occurred in 2015, the Tyndall Glacier has advanced, primarily along its western half. This advance is likely due to submarine deposition of landslide material in front of the glacier. Tidewater glaciers are unstable if the toe of the glacier approaches flotation (e.g., Post et al., 2011). Thus, addition of sediment in
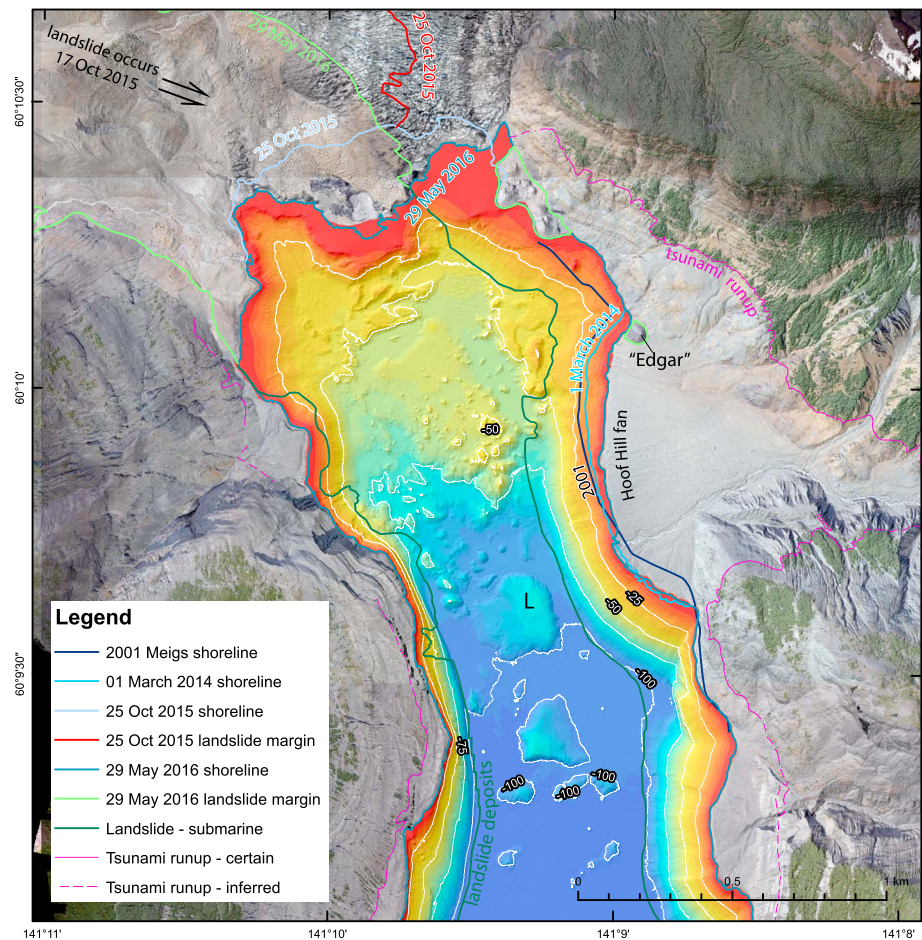
Figure 8. Shaded-relief bathymetry map of the north end of Taan Fiord showing landslide debris on fjord bottom. Warm colors are shallow, and cool colors are deep. Contour interval is 25 m. Shorelines and landslide margins at different times are also shown on the map based on the dates of the imagery acquisition, as well as tsunami runup line. Large block labeled "L" is discussed in the text.

front of the toe of this tidewater glacier allows for it to advance (Brinkerhoff et al., 2017). A comparison of landslide and shoreline positions from 25 October 2015 to 29 May 2016 shows how the glacier advanced by up to 300 m (Figures 8 and 9). The area of up to 70-m shoaling in front of the glacier face is the greatest reduction in water depth in the entire map area (Figure 9), which is proximal to part of the landslide. The correlation of this shoaling with the southward advance of the glacier indicates that the glacier is plowing the seabed as it advances over recently deposited landslide debris. Around the tip of the Tyndall Glacier, the slope is steep from 0- to 45-m water depths, which suggest that the fjord floor is being deformed to approximately that depth.

3.3. Seismic Stratigraphy and the Submarine Landslide Deposit
3.3.1. Delineation of Seismic Stratigraphy

The seismic reflection data and derivative isopach maps reveal the extent of the submarine landslide deposit (Figures 10–13). Before examining the data from the northern basin, it is helpful to look at the data from the southwestern basin to understand what undisturbed fjord-bottom sediments look like (Figure 10). The acoustic basement is easily mapped on the seismic reflection images (unit AB) and correlates with exposures of the Pliocene glacimarine Yakataga Formation (of Taliaferro, 1932, as modified by Miller, 1957, and Rau et al., 1983) along the shoreline. The seismic data and onland outcrops show that the sill separating the north from the southwestern basins is Yakataga Formation sedimentary rock (Figure 5), not a moraine as suggested by Koppes and Hallet (2006). The nature of the sill suggests that most of the postglacial sediment filling the southwestern basin (sequence PG on Figure 10) was deposited in the interval between about 1963 and
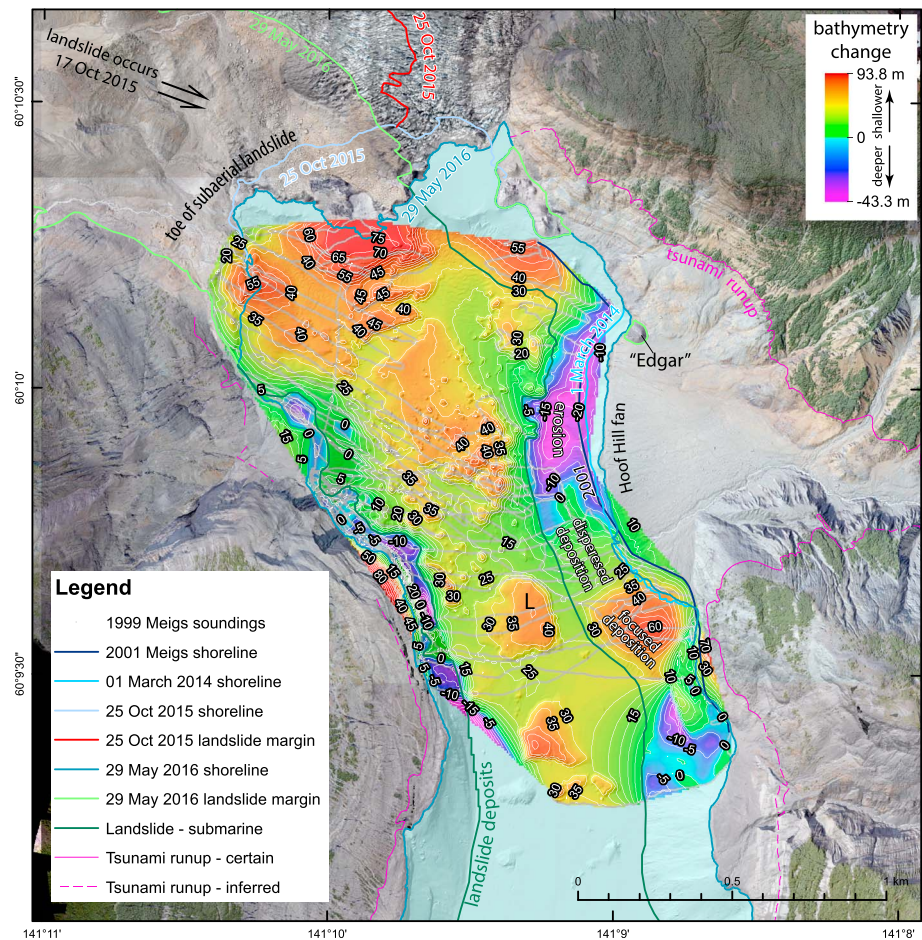
Figure 9. Map of difference in bathymetry by comparing the Meigs et al. (2006) bathymetry collected in 2001 to our bathymetry collected in 2016. The difference values are draped on a shaded-relief bathymetry grid of our 2016 data and are contoured at 5-m intervals. Warm colors, and positive values, indicate shallower depths in the 2016 data; purple colors, and negative values, indicate deeper depths in the 2016 data. Light gray lines show where bathymetry data were collected by Meigs in 2001. The 80-m shallower area along the southwestern edge of the fjord is not real and was caused by an artifact in the contouring algorithm. The 2001 shoreline along the Hoof Hill fan is from Meigs et al. (2006). The 1 March 2014 shoreline along the Hoof Hill fan is from WorldView2 image: WV02_20140301_103001002D519500_103001002E3B9600_seg1. The 25 October 2015 shoreline and outline of the landslide deposit on the glacier are from GeoEye image: GE01_20151025204441_1050010001C98F00_15OCT25204441_P002. The above-sea-level image and the 29 May 2016 shoreline and landslide margin are from the imagery acquired with the LiDAR data we collected (see supporting information S1).

1974 based on the history of glacial retreat. The deepest part of the basin is, on average, 9 m shallower in our 2016 survey than in 1976 (see Figure 4b). The seismic unit PG consists of low-amplitude, acoustically chaotic seismic facies in the deepest part of basin that grades upward and laterally into a seismic facies characterized by laterally continuous, medium- to high-amplitude, horizontal, and parallel reflectors that are slightly wavy and onlap the acoustic basement. In the absence of core data, and based on the seismic facies, we interpret the bottom of unit PG as coarse-grained poorly bedded ice-proximal sediment deposited in the deepest part of this basin. We interpret the upper part of PG as finer-grained ice-distal sediments deposited when the glacier was at, or north of, the 1974 position. The continuity of the upper horizontal reflectors indicates deposition across the entire basin and supports a more distal position of the glacier and sediment source. This entire PG unit is remarkably similar to the deglacial sequence in nearby Muir Inlet in the Glacier Bay region described by Cowan et al. (2010) and in Yakutat Bay described by Zurbuchen et al. (2015). Koppes and Hallet (2006) obtained similar images of the sediments in both the southwest and north basins using a 750-Hz boomer source and interpreted the seismic stratigraphy in the same way (see Figure 3 in their paper).
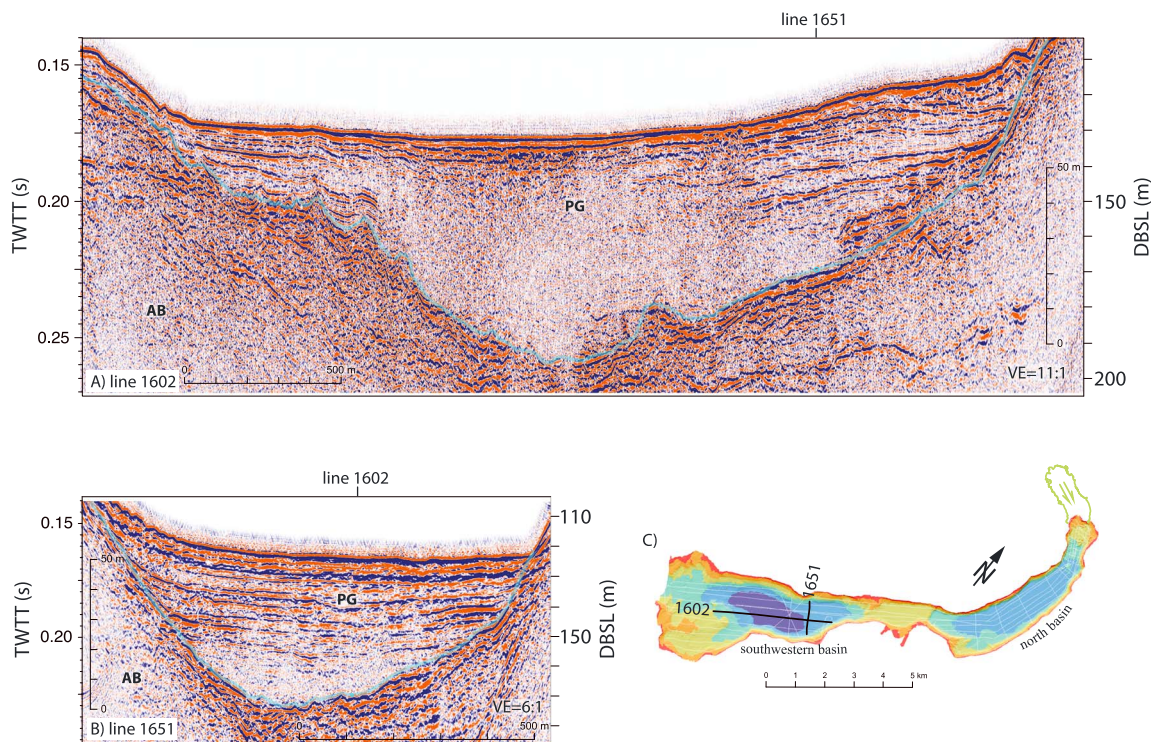
Figure 10. Seismic reflection images of the southwestern basin of Taan Fiord. (a) Part of line 1602. (b) Line 1651. (c) Location map. Unit abbreviations: AB = acoustic basement; PG = postglacial unit. Interpreted horizon is as follows: Light blue line is top of acoustic basement (unit AB) with postglacial unit (unit PG) lying above. For uninterpreted version, see supporting information Figure S2.1. Intersection of lines is shown at the top of each line. Vertical scale on left is two-way travel time (TWTT) in seconds. Vertical scale on right is depth below sea level (DBSL) in meters assuming a velocity of 1,500 m/s. Vertical exaggeration is listed on each section as VE. All sediment above the acoustic basement (light blue line) was deposited between about 1962 and 1983.

An isopach map of this PG unit in the southwest basin reflects the basement topography (Figure 12), and we calculate a total volume of this sediment as 119 ± 3 million cubic meters. To quantify the uncertainty, we combined the vertical resolution and picking errors for the top and bottom of the unit. For the top, which is also the sea bottom, we assign ±1-m resolution and picking errors. For the base, we assign errors of ±3-m resolution and ±8-m picking, although the error is likely less at shallower depths. Additionally, we assign a 25-m uncertainty in the mapped lateral extent. Using an RMS method to combine these uncertainties into a vertical uncertainty, we then multiply this value times the area uncertainty to obtain the volume uncertainty. We find no evidence of unconformities or disconformities in the seismic stratigraphy and thus infer that all sediment was deposited in the 20 years between 1963 and 1974, when the Tyndall Glacier was grounded at each end of the basin. Dividing this volume of sediment by 11 years implies an annual sedimentation rate in this basin of 11,000,000 m^3/year, which is equivalent to a cube of sediment 221 m on each side per year. Comparing the 1976 NOAA bathymetry survey to our 2016 multibeam data shows the basin is on average 9 m shallower, corresponding to a sedimentation rate of 522,000 m^3/year. This lower number suggests a decreasing accumulation rate through time. Using the same methods, Koppes and Hallet (2006) obtained a higher sedimentation rate of 15,000,000 m^3/year for all of Taan Fiord.

This perspective of *normal* fjord sedimentation in the southwestern basin allows us to discriminate and pick the seismic stratigraphy of the northern basin and landslide deposits (Figures 11 and 13). In the north basin, we also image the acoustic basement (unit AB) and unit PG with its facies of moderate to strong amplitude parallel and horizontal reflectors. We found it straightforward to map unit AB beneath the southern part of the fjord but difficult to map deep beneath the northern part of the fjord, where the landslide blocks likely act to disperse acoustic energy. Sequence PG is only clearly imaged at the southern end of the basin and on the margins, but it certainly extends at depth to the north. PG is overlain by a deposit that includes the landslide blocks that protrude above the sea bottom (Figure 11). We infer this is a *blocky* landslide deposit and refer to it as unit BL. This unit has a seismic facies of moderate to strong amplitude, often chaotic
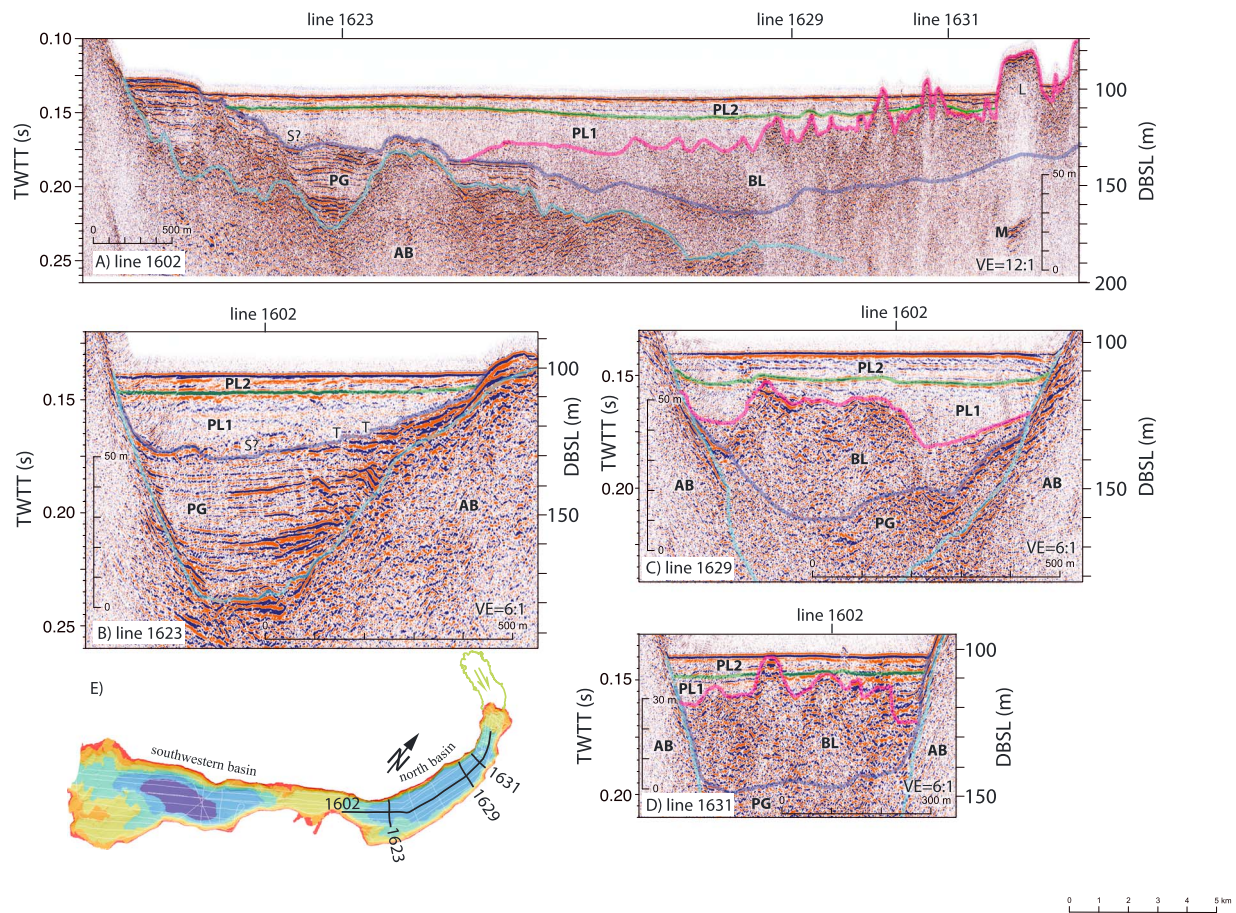
Figure 11. Interpreted seismic reflection images of the north basin of Taan Fiord. Uninterpreted lines are shown in supporting information Figure S2.2. (a) Northern part of line 1602. (b) Line 1623. (c) Line 1629. (d) Line 1631. (e) Location map. Unit abbreviations: AB = acoustic basement; PG = postglacial unit; BL = blocky landslide unit; PL1 = postlandslide unit 1; PL2 = postlandslide unit 2; M = water-bottom multiple. Interpreted lines are as follows: Light blue line is top of acoustic basement (unit AB), dark blue line is top of postglacial sediment (unit PG); pink line is top of blocky landslide unit (unit BL), and green line is top of postlandslide unit 1 (unit PL1) with postlandslide unit 2 (unit PL2) lying above. For uninterpreted version, see supporting information Figure S2.2. The intersection of lines is shown at the top of each line. Vertical scale on left is two-way travel time (TWTT) in seconds. Vertical scale on right is depth below sea level (DBSL) in meters assuming velocity of 1,500 m/s. Vertical exaggeration is listed on each section as VE. Label "T" on line 1631 shows truncations of the postglacial sequence strata. Label "S?" on lines 1602 and 1623 is possible fjord-bottom sediment shoved laterally during the landslide.

reflections, which locally show convoluted and dipping reflectors. The top of this unit is easiest to image toward the north end of the basin, where the multibeam bathymetry images the landslide blocks and where the tops of these blocks can be easily imaged below the sea bottom in the seismic data. Precisely tracing the top of unit BL southward on profiles along the length of the basin (such as line 1602, Figure 11), becomes more difficult. The top of unit BL is least certain between crossline 1629 (Figures 11a and 11c) and the toe of the submarine landslide deposit; however, the higher amplitude reflections in this sequence allow the BL unit to be traced southward to where it overlies the PG unit within about 5 m vertically. It is more difficult to interpret the base of BL in the northern part of the fjord beneath the blocks (for example, the west side of line 1629, Figure 11c), likely due to the scattering of acoustic energy off the blocks within the deposit. Between the blocks, there are sometimes high amplitude reflections tens of milliseconds below the sea bottom, which we infer is acoustic basement (AB) resolved due to the greater penetration of seismic energy. By tracing horizons from profile to profile and performing seismic ties, the base of the landslide can be reasonable and consistent mapped throughout the basin, except for the northernmost kilometer of the fjord. In the northernmost part of the fjord, we utilized Meigs' 2001 bathymetry as a guide for the base of the blocky landslide unit. We estimate that we have picked the top to within 5 m and the bottom of the blocky landslide unit within 5–10 m of the true depth.
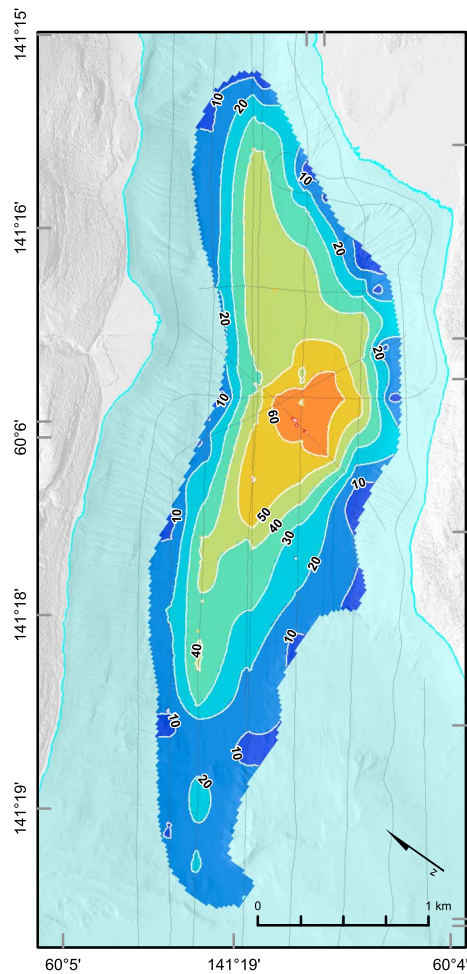
Figure 12. Isopach map of depth to acoustic basement in the southwestern basin of Taan Fiord. Ten-meter contour interval.

We divided the post-blocky landslide seismic stratigraphy into two units (Figures 11 and 13c–13e). The lowest postlandslide unit is PL1. The top of this unit has a bright, subhorizontal, high-amplitude reflector, which can easily and very confidently be traced around the basin. The only uncertainty in picking the base of Unit PL1 was near the toe of the blocky landslide deposit (Unit BL), but an increase in the amplitude of the reflections within unit BL helps to narrow down the unit contact to within about 5 m. The uppermost postlandslide unit is PL2, which has the prominent high-amplitude reflector at its base. It is traceable throughout much of the north basin and does not exist in the southwestern basin. We are highly confident in all contacts for this unit and thus assign a picking error equivalent to the resolution with 1 m for the top of PL2 and 2 m for the base of PL2/top of PL1.

To quantify uncertainty, as described above, we combine the vertical resolution and picking errors for the top and bottom of each of the three units. For unit PL2, the top, which is also the sea bottom, has ±1-m resolution and picking errors. For the base of PL2 and top of PL1, we assign ±2-m resolution and picking errors. For the base of PL1 and top of BL we assign ±2-m resolution and ±5-m picking. Lastly, for the base of unit BL we assign errors of ±3-m resolution and ±10-m picking. Additionally, we assign a 25-m uncertainty in the lateral extent of each of these units. Using an RMS method, we combine these uncertainties into a vertical uncertainty, and we then multiply these values times the area uncertainty to obtain the volume uncertainty listed in Table 1. All volumes assume a minimum velocity (1,500 m/s) and thus could be 10–20% greater in thickness if the sediments undergo dewatering and compaction during transport. The volume uncertainties are 3.3% for unit PL2, 4.0% for unit PL1, and 5.9% for unit BL. These combined uncertainties are small relative to the total volumes.

3.3.2. Interpretation of Seismic Stratigraphy

The seismic lines and the resulting isopach maps (Figures 11 and 13) show that the landslide (unit BL) and postlandslide sediment that overlie unit BL (units PL1 and PL2) extend throughout the northern basin (Figure 13a). This blocky landslide unit has a long tongue more than 30 ± 12 m thick that extends 3 to 4 km downfjord from where the landslide debris entered the water. The blocky debris of unit BL extends about 4.5 km from the where the landslide entered the water (Figure 13b). The thickest part of the landslide deposit (>60 ± 12 m thick) is on top of a block that protrudes above the sea bottom.

The two post-blocky landslide deposits have different depositional patterns reflecting different depositional processes (Figures 11 and 13). In the upper 10–15 ms of the lower postlandslide unit (PL1) are subhorizontal low-amplitude and long-wavelength reflections (Figure 11). These reflectors remain subparallel to the seafloor even around landslide blocks that extend above the sea bottom. The reflectors also lap onto, and do not drape, basement, indicating they are a result of postlandslide gravity-driven deposition rather than slow settling out of the water column. The basal seismic stratigraphy of the unit, particularly in the more distal part of the slide, is acoustically transparent and chaotic with low-amplitude reflections, but it also truncates horizons in the postglacial unit (PG, see "T" labels on line 1623 on Figure 11). This truncation implies erosion by the PL1 flow across the PG sediments. More coherent, but wavy, reflectors in parts of the distal PG unit, just below the base of PL1, may be somewhat intact, postglacial strata deformed by rapid emplacement of PL1 (see "S?" labels on lines 1602 and 1623 on Figure 11). The differences between the top and bottom of unit PL1 bring into question if it should be split apart. We were able to divide PL1 into two subunits, but given an apparently gradational nature between the upper and lower parts of this unit, we conclude it should be considered part of the same unit in terms of depositional process. The isopach map shows the thickest part of unit PL1 (>30 m) lies in the southern half of the basin, adjacent to the thicker, and shallower parts, of unit BL (Figure 13c). Thus, the PL1 unit was filling the deeper parts of the basin after emplacement of unit BL, indicating that gravity was a driving factor in its deposition. Given the evidence for gravity-driven deposition and
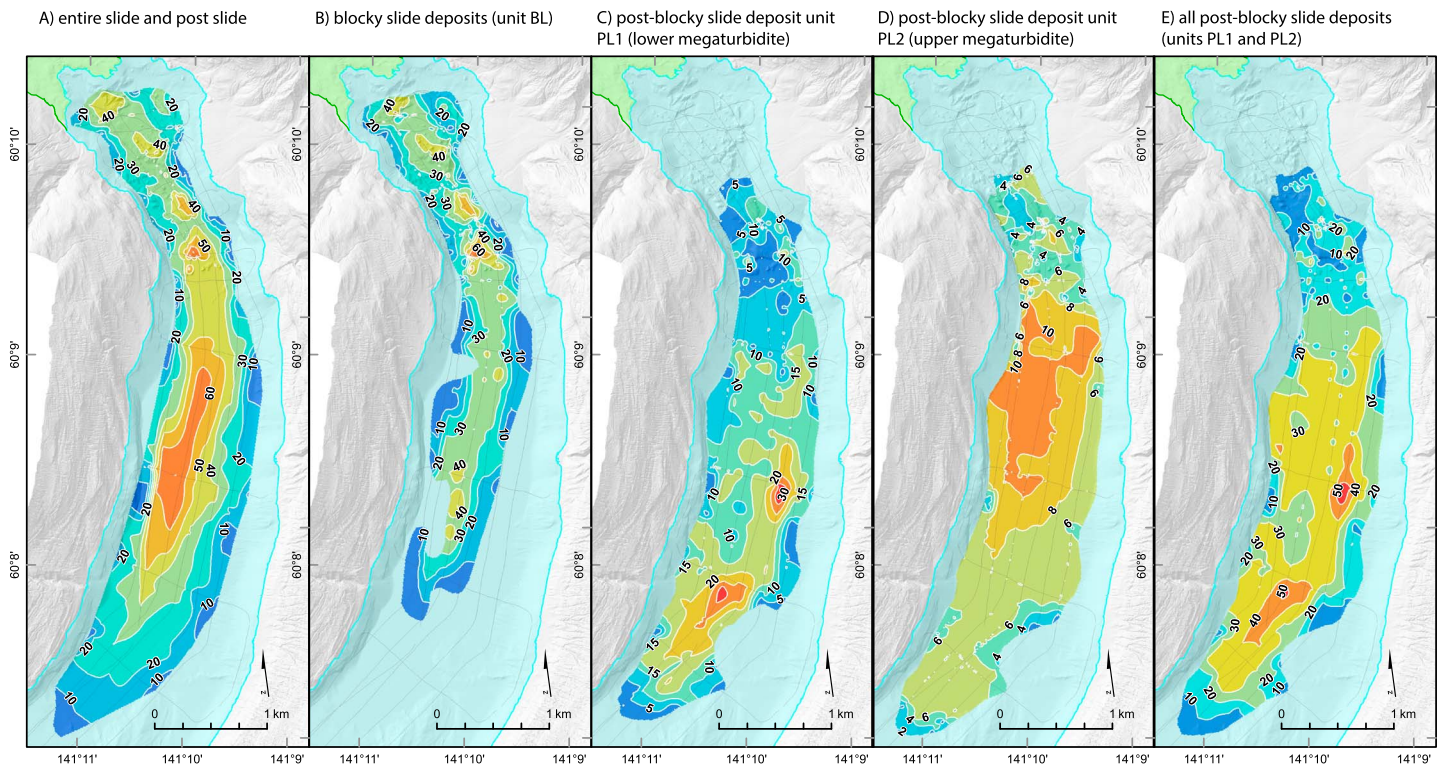
Figure 13. Isopach maps of seismic stratigraphic units in the northern basin of Taan Fiord. Onland area of landslide shown in light green. (a) Thickness of all slide and postslide deposits. (b) Thickness of all blocky landslide debris, unit BL on seismic profiles of Figure 11. (c) Total thickness of postlandslide unit 1 (PL1). (d) Total thickness of postlandslide unit 2 (PL2), which we interpret as a megaturbidite. (e) Total thickness of all post-blocky landslide debris.

a single depositional package with an upward transition from acoustically transparent to low-amplitude long-wavelength reflectors, we interpret this as a gravity flow deposit (Postma, 1986). Although we lack fjord-bottom cores to observe it, we infer this is likely a megaturbidite given the rapid deposition of landslide and the almost certain role of hydrodynamic sorting of sediment during deposition. The unit fits the qualifications of the term *megaturbidite* as defined by Bouma (1987) in that it is thick relative to other units, laterally extensive, interpreted to be different in composition, and lacking in submarine fan morphologies.

The uppermost post landslide unit (PL2) is relatively thin (<12 m) and uniform in thickness when compared to unit PL1 (Figure 13). The isopach map shows the unit is consistently six or more meters thick, with the thickest part in the northern part of the deposit area (Figure 13d). The base of this unit is not deflected around blocks that emerge above the sea bottom (see line 1602, Figure 11). This relationship indicates this unit was not deposited by settling out of the water column, but it is also a gravity flow deposit (Postma, 1986). There is no evidence of truncation of reflectors at its base indicating that deposition of unit PL2 was not erosive, suggesting that it was perhaps lower density and grainflow was hydrodynamically supported. We also note that the sea bottom is flatter and more horizontal than the base of this unit (see line 1602, Figure 11), also suggesting low viscosity during deposition. These observations lead us to interpret this is likely a turbidity deposit, and given a thickness of 6–12 meters (Figure 13d) we infer this is also a megaturbidite, as it meets the conditions of the term as described in the previous paragraph (Bouma, 1987).

4. Dynamics of an STS Landslide

Interpretation of the combined bathymetric, topographic, and seismic data give a clearer picture of landslide processes and deposition. A comparison of the volumes of the submarine parts of the slide debris determined from seismic data (Table 1) shows that the total volume of the slide and postslide material (147,000,000 m^3) is about 3 times the calculated volume of material that entered the fjord (51,000,000 m^3). Thus, a volume of fjord-bottom sediment that was nearly twice the volume of the subaerial landslide

material was incorporated into the slide and postslide deposits during the event. Displacement or incorporation of fjord-bottom material into the slide is also indicated by the base of the blocky landslide unit (unit BL) lying up to 15 m below the base of the prelandslide fjord bottom (from the data collected in 2001 by Meigs et al., 2006). Given the blocky nature of unit BL (on Figures 11 and 13b), this part of the deposit consists dominantly of Yakataga Formation blocks derived from the subaerial slide scar. The one exception to this is the large, flat-topped block with rounded edges labeled "L" on Figures 6, 8, 9, and 11 (line 1602), which might be a mobilized, but intact piece of fjord-bottom sediment. The seismic reflection data did not reveal any particularly distinctive features of this block relative to the others. Regardless, as the volume of the blocky slide material (unit BL) is 128% of the volume of the material that entered the fjord, and it seems certain that the blocky unit consists dominantly of Yakataga Formation slump blocks with a smaller percentage of fjord-bottom sediment. The proximal part of the submarine landslide deposit has numerous large blocks (greater than tens of meters across) as seen on the bathymetry data (Figure 4; see line on Figure 13b; see also Dufresne et al., 2017, Figure 6), but the distal part of the unit seems to have no large blocks, although it is in the same seismic-stratigraphic unit, and thus, perhaps there was more fjord-bottom sediment incorporated into the distal deposit. The amplitude of the chaotic reflections within unit BL decreases near the toe of the slide, suggesting a lower acoustic impedance contrast and thus lower density, which supports this interpretation.

There is some uncertainty about the timing and modes of deposition of the post-blocky landslide units (PL1 and PL2). The planar reflectors in the post-blocky landslide units (PL1 and PL2) are not deflected by, nor drape, emergent landslide blocks. We thus infer rapid and sequential deposition of each of these two units by sediment gravity flows rather than slower settling out of hydrodynamically suspended sediment in the days to weeks following the landslide. The deeper PL1 unit, which is thickest in the distal and eastern parts of the slide, fills low areas after deposition of the blocky landslide unit (BL). The volume of the PL1 unit (46,000,000 m^3) is similar to the volume of the sediment that entered the fjord (51,000,000 m^3) suggesting that the blocky landslide material (unit BL) was able to provide enough energy to result in a similar volume of fjord sediment being suspended into the water column and/or captured in a turbulent flow as the landslide progressed downfjord. The upper PL2 unit has a very different isopach pattern with mostly uniform deposition throughout the deepest part of the basin. However, it is somewhat thicker in the middle part of the basin with a relatively flat and horizontal upper surface (Figure 13). The prominence of the reflector between PL1 and PL2, and the lack of truncation of PL1 reflectors, indicates some period of time between deposition of the two units. One clue to timing is a satellite image of the fjord from 8 days after the landslide showing normal blue water in the fjord. There is no gray or brown water that would indicate higher-than-normal suspended sediment, except along the shoreline adjacent to the landslide (see Figure 12 of Dufresne et al., 2017, for part of the image). Many large landslides continue to experience smaller slope failures after the main movement occurs (e.g., Carson, 1977; Hungr et al., 2001), thus significant pulses of failed sediment may have followed the main slide in seconds to days afterward. We suggest that one reasonable scenario is that after the main blocky landslide material entered the fjord, it eroded and entrained weak water-saturated (Hutchinson & Bhandari, 1971) fjord floor sediment in the slide. As the slide mass encompassed and mixed the finer-grained fjord floor sediment, it traveled along the fjord bottom and suspended additional sediment in the water column. After the blocks settled into position, unit PL1 was rapidly deposited as a fully liquefied laminar debris flow or as a graded turbidite, with the lowermost part of the unit being coarser grained and quicker to settle. As the water velocity decreased, and after passage of the landslide-induced tsunami, the upper part of unit PL1 was deposited by some combination of settling and additional turbidity flows, giving rise to the low-amplitude reflections on the seismic data. The upper, and thinner, megaturbidite, PL2, may be related to subsequent retrogressive failure of the subaerial slide scarp, which would introduce additional sediment into the fjord and possibly combine with seiching within the basin that had a resonant period of about 40 min (Higman et al., 2018). Perhaps the uppermost part of unit PL2 is related to rapid settling of somewhat finer-grained sediment as seiching subsided. Another possibility is that units PL1 and PL2 are related to multiple surges of a single debris flow (Mohrig et al., 1998). However the strong reflector between the two units perhaps suggests more time between deposition of the two units. Coring would help clarify the origins of these two units. Given the lack of evidence for significant sediment in the water column on the satellite image 8 days after the event, we infer settling of finer-grained sediment was complete within the first week after the event.

Table 2
Comparison of Alaskan Submarine Landslides and Taan Fiord STS Landslide

Characteristic	Alaskan submarine landslides	Taan Fiord STS landslide
Shape of slide front	lobate front	pointed front
Upper slide surface	uniform	variable
Slide thickness	up to 20 m	up to 70 m
Lateral shape	uniform	thicker toward middle
Percentage of blocks	low to moderate	high
Block shape	subrounded	angular to sub angular
Seismic signature	chaotic to transparent, low amplitude	chaotic, moderate to high amplitude
Erosive?	yes	yes
Nature of postslide deposits	sometimes thin (<4 m) distal turbidite	megaturbidites (to 40 m) overlying slide
Volume of postslide deposits	small	>100% of blocky slide material
Seismic signature of postslide deposits	can be difficult to identify in water-bottom double pulse from sparker source	distinctive high-amplitude long-wavelength reflections in thick unit

Note. STS = subaerial-to-subaqueous.

The Taan Fiord STS landslide was remarkably well characterized by earthquake seismology. Our estimate of the landslide volume of 76,000,000 m^3 is slightly larger than earlier estimates that did not include the material remaining in the slide scar. Assuming a Yakataga Formation density of 2,350 kg/m^3, based on rocks of similar age and burial history in the Cook Inlet region (Mankhemthong et al., 2013; Saltus et al., 2016), the slide mass was 177.9×10^9 kg. The seismologically determined estimate of 100–150 billion kilograms for the mass of the deposit is remarkably close to our estimate of the landslide mass (Higman et al., 2018). The seismological estimate of the slide direction was toward 096°, and the estimate of the slide direction based on imagery is 114°. As there are few examples where the seismological estimate of slide mass is compared to on-ground measurements, this agreement provides validation that seismological estimates of slide mass and direction are reasonable.

5. Signature of an STS Landslide Discussion

The submarine geologic record of the Taan Fiord STS landslide is profound. There was deposition of 10 to 60 m of sediment, including lithified blocks, throughout the entire north basin as a result of the landslide. The landslide blocks are easily imaged on the bathymetry data as well as the seismic data. The post-blocky landslide deposits are distinct from typical fjord sedimentation in having long-wavelength moderate-amplitude reflectors. The ability of the STS landslide to incorporate ~2 times the subaerial slide volume of fjord-bottom sediment makes the geologic record more obvious and possibly contributes to tsunami generation as the landslide volume grows during the event. The Taan Fiord data also show the importance of utilizing both seismic and bathymetry data to study the submarine landslide, as the extent of the deposit is much larger than indicated by bathymetry data alone.

There are significant differences in the deposits of this STS landslide with purely submarine landslides in other Alaskan fjords (Table 2; see Brothers et al., 2016; Haeussler et al., 2007, 2013; Lee et al., 2006, 2007; Parsons et al., 2014; Ryan et al., 2010). As discussed earlier, submarine landslide deposits tend to have a broad lobate front, in contrast to the more pointed front of the Taan Fiord deposit. These submarine landslide deposits tend to have a uniform thickness, commonly in the range of 10–20 m. Their upper surface can be blocky, but the number of large angular blocks is not nearly as high nor are they as angular as this STS landslide deposit, because those blocks consist of submarine fan sediments or sometimes till. The acoustic signature of the submarine landslide deposits is also commonly acoustically chaotic or transparent. As the sediment consists of unlithified material, the amplitude of the reflections is lower than in the Taan Fiord deposit, which consists of poorly lithified bedrock. Some submarine landslide deposits have localized turbidites in the distal parts of the landslide basin, but there is no evidence for a thick (>5 m) capping mudflow or megaturbidite, such as units PL1 and PL2 in Taan Fiord. Therefore, if the submarine characteristics of other STS landslides can be generalized from the Taan Fiord example, they should be readily identified in other fjords. The thickness of the deposit, the rugged top surface, the post-blocky material deposits, and the acoustic signature are all distinctive and should allow identification of this type of landslide (Table 2).

There are some similarities in inferred landslide processes of the Taan Fiord deposit to the purely submarine landslide deposits in other Alaskan fjords. All the purely submarine landslides are erosive (Brothers et al., 2016; Haeussler et al., 2007, 2013; Lee et al., 2007; Parsons et al., 2014; Ryan et al., 2010), as well as for the Taan Fiord landslide. Moreover, the purely submarine landslides can incorporate a significant volume of material, bulk up, and make the deposit volume up to about twice the source slide area volume (in particular, see Haeussler et al., 2007; Ryan et al., 2010) similar to our results here. However, the relative volume of the Taan Fiord slide deposit is about three times the volume of material that entered the water, in contrast to the submarine landslide deposits that typically have a much smaller percentage of incorporated material.

The proximity of the Taan Fiord STS landslide to the tidewater Tyndall Glacier could either help preserve or erase the submarine deposit from the geologic record. The advance of the Tyndall Glacier over the slide debris in the 6 months after the landslide, and the deformation of the fjord-floor sediments adjacent to the glacier (Figure 9) could act to erase or obfuscate the STS landslide from the submarine record. If colder climate caused the glacier to advance down the fjord, it would erase the record of the landslide. Alternatively, with continued glacial retreat, the STS landslide may be preserved in the geologic record.

Finally, we anticipate the Taan Fiord landslide and tsunami should become a benchmark example for landslide-generated tsunami models. The postlandslide bathymetry and topography data are excellent in quality and resolution, and the combined topography and bathymetry data set that we present should be useful. Also, the subaerial landslide volume and the volume that entered the water are tightly constrained. The volumes of the submarine landslide deposits are reasonably constrained. Although the prelandslide fjord bathymetry is not high resolution, the Meigs et al. (2006) data for the north end of the north basin appear reliable and usable. Tsunami runup elevations are well constrained from imagery and field observations (Higman et al., 2018), and tsunami flow directions are easily observed from impacted vegetation (see supporting information S4). These data should make the Taan Fiord landslide a straightforward test case for landslide-tsunami models.

References

Aarseth, I., Lønne, Ø., & Giskeødegaard, O. (1989), Submarine slides in glaciomarine sediments in some western Norwegian fjords. *Marine Geology*, *88*(1–2), 1–21. https://doi.org/10.1016/0025-3227(89)90002-9

Barclay, D. J., Barclay, J. L., Calkin, P. E., & Wiles, G. C. (2006). A revised and extended Holocene glacial history of Icy Bay, southern Alaska, USA. *Arctic, Antarctic, and Alpine Research*, *38*(2), 153–162. https://doi.org/10.1657/1523-0430(2006)38[153:ARAEHG]2.0.CO;2

Bardet, J.-P., Synolakis, C. E., Davies, H. L., Imamura, F., & Okal, E. A. (2003). Landslide tsunamis: Recent findings and research directions. *Pure and Applied Geophysics*, *160*(10-11), 1793–1809. https://doi.org/10.1007/s00024-003-2406-0

Bøe, R., Rise, L., Blikra, L. H., Longva, O., & Eide, A. (2003). Holocene mass-movement processes in Trondheimsfjorden, Central Norway. *Norwegian Journal of Geology*, *83*, 3–22. ISSN 029-196X

Bouma, A. H. (1987). Megaturbidite: An acceptable term? *Geo-Marine Letters*, *7*(2), 63–67. https://doi.org/10.1007/BF02237985

Brinkerhoff, D., Truffer, M., & Aschwanden, A. (2017). Sediment transport drives tidewater glacier periodicity. *Nature Communications*, *8*(1), 90. https://doi.org/10.1038/s41467-017-00095-5

Brothers, D. S., Haeussler, P. J., Liberty, L., Finlayson, D., Geist, E., Labay, K., & Byerly, M. (2016). A submarine landslide source for the devastating 1964 Chenega tsunami, southern Alaska. *Earth and Planetary Science Letters*, *438*, 112–121. https://doi.org/10.1016/j.epsl.2016.01.008

Cai, J., Powell, R. D., Cowan, E. A., & Carlson, P. R. (1997). Lithofacies and seismic-reflection interpretation of temperate glaciomarine sedimentation in Tarr Inlet, Glacier Bay, Alaska. *Marine Geology*, *143*(1-4), 5–37. https://doi.org/10.1016/S0025-3227(97)00088-1

Carson, M. A. (1977). On the retrogression of landslides in sensitive muddy sediments. *Canadian Geotechnical Journal*, *14*(4), 582–602. https://doi.org/10.1139/t77-059

Cowan, E. A., Seramur, K. C., Powell, R. D., Willems, B. A., Gulick, S. P. S., & Jaeger, J. M. (2010). Fjords as temporary sediment traps: History of glacial erosion and deposition in Muir Inlet, Glacier Bay National Park, southeastern Alaska. *Geological Society of America Bulletin*, *122*(7–8), 1067–1080. https://doi.org/10.1130/B26595.1

Dufresne, A., Geertsema, M., Shugar, D. H., Koppes, M., Higman, B., Haeussler, P. J., et al. (2017). Sedimentology and geomorphology of a large tsunamigenic landslide, Taan Fiord, Alaska. *Sedimentary Geology*, *364*, 302–318. https://doi.org/10.1016/j.sedgeo.2017.10.004

Ekström, G., & Stark, C. P. (2013). Simple scaling of catastrophic landslide dynamics. *Science*, *339*(6126), 1416–1419. https://doi.org/10.1126/science.1232887

Elliott, J., Freymueller, J. T., & Larsen, C. F. (2013). Active tectonics of the St. Elias orogen, Alaska, observed with GPS measurements. *Journal of Geophysical Research: Solid Earth*, *118*, 5625–5642. https://doi.org/10.1002/jgrb.50341

Enkelmann, E., Koons, P. O., Pavlis, T. L., Hallet, B., Barker, A., Elliott, J., et al. (2015). Cooperation among tectonic and surface processes in the St. Elias Range, Earth's highest coastal mountains. *Geophysical Research Letters*, *42*, 5838–5846. https://doi.org/10.1002/2015GL064727

George, D. L., Iverson, R. M., & Cannon, C. M. (2017). New methodology for computing tsunami generation by subaerial landslides: Application to the 2015 Tyndall Glacier landslide, Alaska. *Geophysical Research Letters*, *44*, 7276–7284. https://doi.org/10.1002/2017GL074341

Grämiger, L. M., Moore, J. R., Gischig, V. S., Ivy-Ochs, S., & Loew, S. (2017). Beyond debuttressing: Mechanics of paraglacial rock slope damage during repeat glacial cycles. *Journal of Geophysical Research: Earth Surface*, *122*, 1004–1036. https://doi.org/10.1002/2016JF003967

Gulick, S. P. S., Reece, R. S., Christeson, G. L., van Avendonk, H., Worthington, L. L., & Pavlis, T. L. (2013). Transition fault and the unstable Yakutat-Pacific-North American triple junction. *Geology*, *41*(5), 571–574. https://doi.org/10.1130/G33900.1

Haeussler, P., Lee, H., Ryan, H., Labay, K., Kayen, R., Hampton, M., & Suleimani, E. (2007). Submarine slope failures near Seward, Alaska, during the M9.2 1964 earthquake. In V. Lykousis, D. Sakellariou, & J. Locat (Eds.), *Submarine Mass Movements and their Consequences*, (Vol. 27, pp. 269–278). Dordrecht, Netherlands: Springer. https://doi.org/10.1007/978-1-4020-6512-5_28

Haeussler, P. J., Parsons, T., Finlayson, D., Hart, P., Chaytor, J., Ryan, H., et al. (2013). New imaging of submarine landslides from the 1964 earthquake near Whittier, Alaska, and a comparison to failures in other Alaskan fjords. In S. Krastel (Ed.), *Submarine mass movements and their consequences, Advances in Natural and Technological Hazards Research* (Vol. *37*). Dordrecht, Netherlands: Springer. https://doi.org/10.1007/978-3-319-00972-8

Hamilton, E. L. (1969). Sound velocity, elasticity, and related properties of marine sediments, North Pacific. *Naval Undersea Research And Development Center, Research and Development Report TP 145*, 125 p.

Hampton, M. A., Lee, H. J., & Locat, J. (1996). Submarine landslides. *Reviews of Geophysics*, *34*(1), 33–59. https://doi.org/10.1029/95RG03287

Harbitz, C. B., Løvholt, F., Pedersen, G., & Masson, D. G. (2006). Mechanisms of tsunami generation by submarine landslides: A short review. *Norwegian Journal of Geology*, *86*, 255–264. ISSN 029-196X

Higman, B., Shugar, D., Stark, C., Ekström, G., Koppes, M.N., Lynett, P., et al. (2018). Glacier retreat and the largest landslide-triggered marine tsunami since 1958. *Science Advances*, *8*, 12993. https://doi.org/10.1038/s41598-018-30475-w

Hungr, O., Evans, S. G., Bovis, M. J., & Hutchinson, J. N. (2001). A review of the classification of landslides of the flow type. *Environmental & Engineering Geoscience*, *7*(3), 221–238. https://doi.org/10.2113/gseegeosci.7.3.221

Hutchinson, J. N., & Bhandari, R. K. (1971). Undrained loading, a fundamental mechanism of mudflows and other mass movements. *Geotechnique*, *21*(4), 353–358. https://doi.org/10.1680/geot.1971.21.4.353

Jiang, L., & LeBlond, P. (1992). The coupling of a submarine slide and the surface waves which it generates. *Journal of Geophysical Research*, *97*(C8), 12731–12,744. https://doi.org/10.1029/92JC00912

Koehler, R. D. (2013). *Quaternary faults and folds (QFF), Alaska Division of Geological & Geophysical Surveys Digital Data Series* (p. 3). Fairbanks, AK: Alaska Division of Geological and Geophysical Surveys. https://doi.org/10.14509/24956

Koppes, M., & Hallet, B. (2006). Erosion rates during rapid deglaciation in Icy Bay, Alaska. *Journal of Geophysical Research*, *111*, F02023. https://doi.org/10.1029/2005JF000349

Lee, H., Ryan, H. F., Kayen, R. E., Haeussler, P. J., Dartnell, P., & Hampton, M. A. (2006). Varieties of submarine failure morphologies of seismically-induced landslides in Alaskan fjords. *Norwegian Journal of Geology*, *86*, 221–230. ISSN 029-196X

Lee, H. J., Ryan, H. F., Haeussler, P. J., Kayen, R. E., Hampton, M. A., Locat, J., et al. (2007). Reassessment of seismically induced, tsunamigenic submarine slope failures in Port Valdez, Alaska, USA. In V. Lycousis, D. Sakellariou, & J. Locat (Eds.), *Submarine Mass Movements and their Consequences*, (pp. 357–365). Dordrecht: Springer. https://doi.org/10.1007/978-1-4020-6512-5_37

L'Heureux, J. S., Hansen, L., Longva, O., Emdal, A., & Grande, L. (2010). A multidisciplinary study of submarine landslides at the Nidelva fjord delta, Central Norway–implications for geohazards assessments. *Norwegian Journal of Geology*, *90*(1–2), 1–20.

Locat, J., & Lee, H. J. (2002). Submarine landslides: Advances and challenges. *Canadian Geotechnical Journal*, *39*(1), 193–212. https://doi.org/10.1139/T01-089

Mankhemthong, N., Doser, D. I., & Pavlis, T. L. (2013). Interpretation of gravity and magnetic data and development of two-dimensional cross-sectional models for the border ranges fault system, south-Central Alaska. *Geosphere*, *9*(2), 242–259. https://doi.org/10.1130/GES00833.1

Masson, D. G., Harbitz, C. B., Wynn, R. B., Pedersen, G., & Løvholt, F. (2006). Submarine landslides: Processes, triggers and hazard prediction. *Philosophical Transactions of the Royal Society of London A: Mathematical, Physical and Engineering Sciences*, *364*(1845), 2009–2039. https://doi.org/10.1098/rsta.2006.1810

McAdoo, B. G., Pratson, L. F., & Orange, D. L. (2000). Submarine landslide geomorphology, US continental slope. *Marine Geology*, *169*(1-2), 103–136. https://doi.org/10.1016/S0025-3227(00)00050-5

Meigs, A., Krugh, W. C., Davis, K., & Bank, G (2006). Ultra-rapid landscape response and sediment yield following glacier retreat, Icy Bay, southern Alaska. *Geomorphology*, *78*(3–4), 207–221. https://doi.org/10.1016/j.geomorph.2006.01.029

Miller, D. J. (1957). Geology of the southeastern part of the Robinson Mountains, Yakataga district, Alaska. *U.S.* Geological Survey Oil and Gas Investigations Map, OM-187, scale 1:63,360.

Miller, D. J., (1960). Giant waves in Lituya Bay, Alaska. *U.S.* Geological Survey Professional Paper 534-C, 51–83.

Mohrig, D., Whipple, K. X., Hondzo, M., Ellis, C., & Parker, G. (1998). Hydroplaning of subaqueous debris flows. *Geological Society of America Bulletin*, *110*(3), 387–394. https://doi.org/10.1130/0016-7606(1998)110<0387:HOSDF>2.3.CO;2

Nardin, T. R., Hein, F. J., Gorsline, D. S., & Edwards, B. D. (1979). A review of mass movement processes, sediment and acoustic characteristics, and constrains in slope and base-of-slope systems versus canyon-fan-basin floor systens. In L. J. Doyle, & O. H. Pilkey (Eds.), *Geology of continental slopes, Society of Economic Paleontologists and Mineralogists Special Publication*, (Vol. 27, pp. 61–73). https://doi.org/10.2110/pec.79.27.0061

Paguican, E. M. R., van Wijk-de Vries, B., & Lagmay, A. M. (2014). Hummocks: How they form and how they evolve in rockslide-debris avalanches. *Landslides*, *11*, 67–80.

Parsons, T., Geist, E. L., Ryan, H. F., Lee, H. J., Haeussler, P. J., Lynett, P., et al. (2014). Source and progression of a submarine landslide and tsunami: The 1964 great Alaska earthquake at Valdez. *Journal of Geophysical Research: Solid Earth*, *119*, 8502–8516. https://doi.org/10.1002/2014JB011514

Pavlis, T. L., Chapman, J. B., Bruhn, R. L., Ridgway, K., Worthington, L. L., Gulick, S. P., & Spotila, J. (2012). Structure of the actively deforming fold-thrust belt of the St. Elias orogen with implications for glacial exhumation and three-dimensional tectonic processes. *Geosphere*, *8*(5), 991–1019. https://doi.org/10.1130/GES00753.1

Porter, S. C. (1989). Late Holocene fluctuations of the fiord glacier system in Icy Bay, Alaska, USA. *Arctic and Alpine Research*, *21*(4), 364–379. https://doi.org/10.2307/1551646

Post, A. (1983). Preliminary bathymetry of upper Icy Bay, Alaska. *U.S. Geological Survey Open-File Report* 83–256, 1 sheet, scale 1:20,000.

Post, A., O'Neel, S., Motyka, R. J., & Streveler, G. (2011). A complex relationship between calving glaciers and climate. *Eos*, *92*(37), 305–306. https://doi.org/10.1029/2011EO370001

Postma, G. (1986). Classification for sediment gravity-flow deposits based on flow conditions during sedimentation. *Geology*, *14*(4), 291–294. https://doi.org/10.1130/0091-7613(1986)14<291:CFSGDB>2.0.CO;2

Rau, W. W., Plafker, G., & Winkler, G. R. (1983). Foraminiferal biostratigraphy and correlations in the Gulf of Alaska Tertiary province. *U.S. Geological Survey Oil and Gas Investigations Chart*, OC-120, 3 sheets, 11 p.

Ryan, H. F., Lee, H. J., Haeussler, P. J., Alexander, C. R., & Kayen, R. E. (2010). In D. C. Mosher, et al. (Eds.), *Submarine mass movements and their consequences, Advances in Natural and Technological Hazards Research*, (Vol. 28, pp. 411–421). Dordrecht, Netherlands: Springer.

Saltus, R. W., Stanley, R. G., Haeussler, P. J., Jones, J. V.,. I. I. I., Potter, C. J., & Lewis, K. A. (2016). Late Oligocene to present contractional structure in and around the Susitna basin, Alaska—Geophysical evidence and geological implications. *Geosphere*, *12*(5), 1378–1390. https://doi.org/10.1130/GES01279.1

Taliaferro, N. L. (1932). Geology of the Yakataga, Katalla, and Nichawak districts, Alaska. *Geological Society of America Bulletin*, *43*(3), 749–782. https://doi.org/10.1130/GSAB-43-749

Ward, S. N. (2001). Landslide tsunami. *Journal of Geophysical Research*, *106*(B6), 11201–11215. https://doi.org/10.1029/2000JB900450

Wood, N. J., & Peters, J. (2015). Variations in population vulnerability to tectonic and landslide-related tsunami hazards in Alaska. *Natural Hazards*, *75*(2), 1811–1831. https://doi.org/10.1007/s11069-014-1399-6

Worthington, L. L., Gulick, S. P. S., & Pavlis, T. L. (2010). Coupled stratigraphic and structural evolution of a glaciated orogenic wedge, offshore St. Elias Orogen, Alaska. *Tectonics*, *29*, TC6013. https://doi.org/10.1029/2010TC002723

Zurbuchen, J. M., Gulick, S. P., Walton, M. A., & Goff, J. A. (2015). Imaging evidence for Hubbard glacier advances and retreats since the last glacial maximum in Yakutat and disenchantment bays, Alaska. *Geochemistry, Geophysics, Geosystems*, *16*, 1962–1974. https://doi.org/10.1002/2015GC005815